EYE-CLIMA
Verifying emissions of climate forcers

Preliminary fluxes of CO_2, CH_4 and N_2O at 0.5° from 2005

DELIVERABLE D3.1

Author(s):	CEA: Grégoire Broquet, Antoine Berchet Science Partners: Audrey Fortems-Cheiney FMI: Maria Tenkanen, Tuula Aalto NILU: Nalini Krishnankutty

Date of submission:	19-09-2024
Version:	1.0
Responsible partner:	NILU
Deliverable due date:	30-06-2024
Dissemination level:	Public

Call:	HORIZON-CL5-2022-D1-02
Topic:	Climate Sciences and Responses
Project Type:	Research and Innovation Action
Lead Beneficiary:	NILU - Norsk Institutt for Luftforskning

This project has received funding from the European Union's Horizon Europe research and innovation programme under grant agreement No 101081395

Document History

Version	Date	Comment	Modifications made by
0.1	16-09-2024	First complete draft	A. Fortems-Cheiney, N. Krishnankutty, G. Broquet, A. Berchet, M. Tenkanen, and T. Aalto
0.2	17-09-2024	Internal review	R. Thompson
0.3	18-09-2024	Final version	A. Fortems-Cheiney, N. Krishnankutty, G. Broquet, A. Berchet, M. Tenkanen, and T. Aalto
1.0	19-09-2024	Submitted to Commission	R. Thompson

This project has received funding from the European Union's Horizon Europe research and innovation programme under grant agreement No 101081395

Summary

One of the main objectives of EYE-CLIMA is to use the atmospheric inversion methodology, which can be used to estimate the surface-atmosphere fluxes of various greenhouse gases, to verify and support National Greenhouse Gas Inventories (NGHGIs).

By carrying-out long-term atmospheric inversions of the three most important GHGs, carbon dioxide (CO_2), methane (CH_4) and nitrous oxide (N_2O) for Europe, EYE-CLIMA aims to support the monitoring of emissions for European Union countries (EU27) plus the United Kingdom, Switzerland, and Norway (EU27+3) and provide valuable information for the assessment of emission mitigation policy.

For CO_2, only land biosphere fluxes are optimized in the inversions i.e., net ecosystem exchange (NEE), while for CH_4 and N_2O fluxes from all sectors are optimized. This report provides details on inversions performed for CO_2, CH_4, and N_2O, and is a precursor to a second report (due in 2025), in which the inversions will be run from 2005 to at least 2023.

The inversions of CH_4 and N_2O are at weekly and monthly temporal resolution, respectively, while for CO_2, the inversions have a temporal resolution of monthly with a sub-daily time step of 6 hours to allow the diurnal cycle in CO_2 fluxes to also be optimized. These inversions are based on observations from ground-based sites (e.g., from ICOS, INGOS, GAW, and NOAA networks) with long-term records for consistency overall years. For CO_2, additional inversions were performed using satellite observations from OCO-2. For the inversions, prior flux information is obtained from Work Package 2, along with other global emission estimates. Inversions are computed with two different inversion frameworks: the Community Inversion Framework (CIF) combined with CHIMERE and FLEXPART for CO_2 and N_2O respectively, and CTDAS-TM5 for CH_4. The boundary conditions for the regional simulations are global optimized fields of mixing ratios, choosing the product for each species that contributes the least error.

The spatial resolution of CO_2 and N_2O fluxes are 0.5°×0.5° and for CH_4 it is 1°×1°. Presently, CO_2 inversions using surface measurements have been performed for the period 2005-2022 while the inversions using satellite observations have been conducted for the period 2015-2019. For N_2O and CH_4, the inversions are performed for the period 2015-2020 and 2016-2021 respectively.

For CH_4, the optimized fluxes resulted in a notable improvement in the agreement with the observations and indicated a 24.6% increase in annual emissions compared to prior estimates, largely driven by larger anthropogenic sources. Emissions were concentrated in central and southern Europe, with a strong emission peak in the land biosphere source in late summer and a maximum in the anthropogenic emissions in August.

For N_2O, the forward transport model run with the optimized fluxes showed an improved agreement with the observations compared to using the prior fluxes. The inversion resulted in increased emissions in the Netherlands, Germany, and the UK, while decreases were observed in parts of France and Southern Europe. The emissions also displayed a seasonal cycle with a maximum in early summer. These preliminary inversions also indicate higher emissions in 2019 and 2020 compared to earlier years.

For CO_2, the inversions using surface measurements and OCO-2 satellite observations both significantly improved the fit between the simulated and observed CO_2 concentrations. European ecosystems act as CO_2 sinks, though there remains variability in the annual estimates of the terrestrial ecosystem fluxes, mainly due to uncertainties in the atmospheric transport modeling and boundary conditions. These results highlight the need for further refinement of NEE estimates.

This project has received funding from the European Union's Horizon Europe research and innovation programme under grant agreement No 101081395

TABLE OF CONTENTS

This project has received funding from the European Union's Horizon Europe research and innovation programme under grant agreement No 101081395

This project has received funding from the European Union's Horizon Europe research and innovation programme under grant agreement No 101081395

1. Introduction

To mitigate global warming, the emissions of greenhouse gases (GHGs) need to be reduced. Up to present, the standard method to monitor GHG emissions has been the use of national greenhouse gas inventories (NGHGIs), which are typically compiled using activity data and emission factors. However, NGHGIs contain uncertainties due to uncertainty in the emission factors as well as in the activity data.

One of the main objectives of EYE-CLIMA is to provide independent verification of NGHGIs by developing top-down methods based on atmospheric inversion to a level of readiness where they can be used to determine emissions at national and sub-national scales.

This deliverable presents the first atmospheric inversion results for the three main GHGs, carbon dioxide (CO_2), methane (CH_4) and nitrous oxide (N_2O) for Europe, and is a precursor to the final inversions, which will be run from 2005 up to at least 2023. This long timeseries of observation-based emissions estimates will provide valuable information on the trends in the emissions and help support policy decisions regarding emission mitigation.

Atmospheric inversion is a way to use atmospheric observations, e.g., mixing ratios of GHGs, to estimate surface-atmosphere fluxes and their uncertainties. The method involves using an atmospheric chemistry transport model (ACTM) to relate an existing independent estimate of the fluxes (the prior estimate) to atmospheric mixing ratios and to determine the model-observation error. This error is then used to update the prior estimate by effectively inverting the transport to relate the difference in mixing ratio to a difference in flux.

The 0.5°×0.5° resolution inversion used in this deliverable (except for CH_4 for which 1°×1° resolution has been used) is assumed to be sufficient to reliably estimate the annual country totals for mid to large European countries, is indeed the typical resolution of inverse systems for estimating GHG budgets at the European scale. Moreover, due to the sparsity of observations in the 2000s and up to the start of the ICOS network, it is not possible to reliably constrain the emissions at higher resolution over the entire target time period. As a primary step towards the long-term inversions (from 2005 to at least 2023), preliminary CO_2, CH_4 and N_2O inversions have been run, which cover a shorter time period, but provide a good indication of how well the inversions over the whole time period will perform.

2. Methodology

2.1 Inversion framework

Atmospheric inversions work by relating the difference between prior modelled and observed mixing ratios to a correction to the prior flux estimate. In other words, the method minimizes the following cost function $J(\mathbf{x})$ with respect to the state vector $\mathbf{x}$:

$$J(\boldsymbol{x}) = \frac{1}{2}(\boldsymbol{x} - \boldsymbol{x_b})^{\mathrm{T}}\mathbf{B}^{-1}(\boldsymbol{x} - \boldsymbol{x_b}) + \frac{1}{2}(H(\boldsymbol{x}) - \boldsymbol{y})^{\mathrm{T}}\mathbf{R}^{-1}(H(\boldsymbol{x}) - \boldsymbol{y}) \quad (1)$$

Here, $\mathbf{x}$ represents the state vector of model variables, $\mathbf{x_b}$ is the initial guess or prior state vector, $\mathbf{B}$ denotes the background error covariance matrix reflecting uncertainties in $\mathbf{x_b}$, $\mathbf{y}$ is the vector of observed data, $H(\mathbf{x})$ is the observation operator mapping $\mathbf{x}$ to the observation space, and $\mathbf{R}$ is the observation error covariance matrix accounting for uncertainties in $\mathbf{y}$. The first term on the right-hand side of Eq. 1 accounts for deviation from the prior state $\mathbf{x_b}$ and second term represents the observational constraints on the prior fluxes.

To minimize $J(\mathbf{x})$ in CIF-CHIMERE and CIF-FLEXPART, the gradient $\nabla J(\mathbf{x})$ is computed as:

This project has received funding from the European Union's Horizon Europe research and innovation programme under grant agreement No 101081395

$$\nabla J(\boldsymbol{x}) = \mathbf{B}^{-1}(\boldsymbol{x} - \boldsymbol{x_b}) + H'(\boldsymbol{x})\mathbf{R}^{-1}(H(\boldsymbol{x}) - \boldsymbol{y}) \quad (2)$$

The conjugate gradient algorithm (Lanczos, 1950) utilizes $\nabla J(\mathbf{x})$ to iteratively update $\mathbf{x}$, continuing until the gradient norm falls below a predefined threshold or a maximum number of iterations is reached. In CTDAS-TM5, $J(\mathbf{x})$ was minimized using ensemble Kalman filter with 500 ensemble members. (Evensen 2003, Peters et al., 2005).

2.2. Model descriptions

The Community Inversion Framework (CIF) (Berchet et al. 2021) has been used with the atmospheric transport models, CHIMERE and FLEXPART, for inversions of CO_2 and N_2O respectively. For CH_4, the atmospheric inversion framework, CarbonTracker Europe - CH_4 (CTE-CH_4) (Tsuruta et al. 2017) was used.

2.2.1. The Community Inversion Framework (CIF)

The CIF is an open-source Bayesian inversion framework, which was developed under the previous Horizon Europe project, VERIFY. The concept of the CIF is to have a community inversion framework that can be interfaced with multiple atmospheric transport models to enable a consistent inter-comparison of inversions run with different transport operators (Berchet et al. 2021). The CIF has been interfaced with the Lagrangian particle dispersion model, FLEXPART, as well as the regional Eulerian model, CHIMERE, which are used in EYE-CLIMA. Work is also underway to interface CIF with the TM5-MP model, which is also used.

2.2.2. CTE-CH4

We used the global atmospheric inversion model Carbon Tracker Europe - CH_4 (CTE-CH_4, Tsuruta et al., 2017) with TM5 transport model to estimate methane (CH_4) emissions in Europe and globally. CTE-CH_4 framework uses the ensemble Kalman filter approach, which readily provides the flux uncertainties based on the ensemble of flux estimates. CTE-CH_4 estimates CH_4 emissions at a 1° × 1° resolution over Europe at a weekly temporal resolution and optimises anthropogenic and natural emissions separately. Set-up of the model was close to that applied in e.g. Tenkanen et al. (2023).

3. CO_2 inversions

This section describes the preliminary inversions of the CO_2 land ecosystem fluxes in Europe.

The preliminary inversions cover the period 2005 to 2022 and have a 0.5°×0.5° resolution. They rely on a configuration of the CIF-CHIMERE inversion system and on an input database, which are mostly inherited from past projects, but which include the use of estimates of the terrestrial ecosystem fluxes from the first ecosystem model simulations run in the frame of EYE-CLIMA. Different CO_2 inversion results have been derived with this inversion configuration by using different CO_2 terrestrial ecosystem flux simulations in input, and by assimilating surface (mainly from ICOS sites) or satellite (NASA/JPL OCO-2) observations.

This section details the 0.5°×0.5° resolution CIF-CHIMERE inversion configuration, the datasets used for these preliminary inversions experiments and the analysis of the system behaviour and of the resulting land ecosystem flux estimates. In line with the objective of these inversions, which should provide a benchmark for further developments and analysis in EYE-CLIMA, the presentation focuses on general patterns of the spatial variability of the corrections applied to the prior terrestrial ecosystem fluxes from surface and OCO-2 observations, on the seasonal cycle and on the long-term mean, trends and inter-

This project has received funding from the European Union's Horizon Europe research and innovation programme under grant agreement No 101081395

annual variability of annual NEE budget for the European Union + UK area (EU-27+UK), i.e., on the type of general diagnostics analysed in recent inter-comparisons of European scale inversions (Monteil et al., 2020, Thompson et al., 2020, McGrath et al., 2023).

The inversion provides estimates of the Net Biome Productivity (NBP). The final land natural flux estimate from the inversion is mainly complemented by anthropogenic emissions from fossil fuel and by ocean fluxes (even though also by anthropogenic emissions from biofuel combustion), which are not optimised by the inversions, in the transport model when fitting the CO_2 atmospheric observations. Furthermore, it derives NBP by correcting a prior estimate of the land ecosystem fluxes given by NBP from ecosystem model simulations. However, following the traditional labelling in atmospheric inversions, and since the characterization of the uncertainty in this prior estimate is derived from information about the heterotrophic respiration and from studies comparing ecosystem models to ecosystem flux eddy covariance measurements, we will call it Net Ecosystem Exchange (NEE). The main problem for labelling the fluxes derived by the inversions is the ambiguity raised by ignoring fluxes to the atmosphere from inland waters and from harvested wood and crops. McGrath et al., (2023) removed such fluxes from the inversion results for comparisons to ecosystem model simulation of the net CO_2 ecosystem fluxes. Those components will be explicitly accounted for in the future series of reference inversions in D3.2 due in M28 to remove such an ambiguity.

3.1 Inverse modelling system and experimental framework

The inversion system relies on the coupling between the variational mode of the Community Inversion Framework (CIF, Berchet et al., 2021), the regional chemistry transport model CHIMERE (Menut et al., 2013; Mailler et al., 2017) and the adjoint of this model (Fortems-Cheiney et al., 2021b). The specific configuration used here for the inversion of the CO_2 land ecosystem fluxes in Europe is very close to that developed in the frame of the H2020 VERIFY project and documented in McGrath et al. (2023).

3.1.1 Configuration of the regional CHIMERE chemistry-transport model for the simulation of CO_2 mole fractions over Europe

At the time scales considered in this study CO_2 is considered as a passive tracer. Consequently, when using the CHIMERE CTM and its adjoint code, here, only the atmospheric transport modeling components are used, and the chemistry modeling components are disactivated. The CHIMERE domain for Europe covers latitudes 31.75-73.75°N and longitudes 15.25°W -34.75°E with a 0.5°×0.5° horizontal resolution and 17 vertical layers up to 200 hPa. Meteorological forcing for CHIMERE is generated using operational forecasts from the Integrated Forecasting System (IFS) of the European Centre for Medium Range Weather Forecasting (ECMWF).

3.1.2 CO_2 boundary conditions

Initial, lateral and top conditions for CO_2 concentrations at the boundaries of the model and at the simulations initial times are generated from the latest Copernicus Atmospheric Monitoring Service (CAMS) global CO_2 inversions (v22r1) assimilating surface data (Chevallier et al., 2005; Chevallier et al., 2010). This global inversion product is also used to complement the vertical columns of CO_2 above the top boundary of CHIMERE when comparing the model to XCO_2 observations.

Different tests have been performed with or without controlling the initial and lateral conditions.

3.2. Prior fluxes

3.2.1 Prior estimates of the CO_2 land ecosystem fluxes

The principle of the inversion is to correct *a priori* estimates of the net land ecosystem flux maps later referred as “prior" fluxes. Here, two different alternative prior estimates have been used, both coming

This project has received funding from the European Union's Horizon Europe research and innovation programme under grant agreement No 101081395

from simulations with the ORCHIDEE terrestrial ecosystem flux model (Krinner et al., 2005). These two simulations differ in terms of atmospheric forcing:

- the "CRUJRA" prior NBP, from a global ORCHIDEE simulation, provided at a 0.5° resolution from 2005 to 2022 in the framework of the TRENDY model-intercomparison project (Sitch et al., 2015; Friedlingstein et al., 2022)
- the "CRUERA" prior NBP, from a European scale simulation run from 2005 to 2022 in the frame of the EYE-CLIMA project, with a dedicated forcing at the spatial resolution of 0.125°. This prior is described in the Deliverable D2.3 of the EYECLIMA project.

These two priors can present local differences (Figure 3.1) but provide similar seasonal cycles (Figure 3.7) and similar annual budgets (Figure 3.8).

We have aggregated these prior fluxes at the 0.5°x0.5° horizontal resolution of the CHIMERE grid.

3.2.2 Other CO_2 surface fluxes

The other component of CO_2 fluxes from ocean and anthropogenic activities are fixed throughout the inversion. We have aggregated these fluxes at the 0.5°x 0.5° horizontal resolution of the CHIMERE grid.

The anthropogenic fossil fuel and biofuel CO_2 emissions (Gerbig and Koch, 2023) are derived from the spatial distribution of the Emissions Database for Global Atmospheric Research EDGAR-v4.3 inventory (Janssens-Maenhout et al., 2019), on national and annual budgets from the BP (British Petroleum) statistics 2023, and on temporal profiles at hourly resolution derived from the TNO-MACC inventories, following the COFFEE approach (Steinbach et al., 2011). The data is provided from 2005 to 2022 at 0.1°×0.1°horizontal resolution and hourly temporal resolution. For the Deliverable D3.2 at month M28, inversions will be performed with anthropogenic emissions from the EDGARv8 inventory, as recommended by WP2.

The estimate of sea/ocean fluxes within the CHIMERE domain is based on a hybrid product combining the coastal ocean flux estimates from the University of Bergen and a global ocean estimate from MPI-BGC-Jena (Rödenbeck et al., 2014; McGrath et al., 2023). The data is provided from 2005 to 2020 at a 0.125°×0.125° horizontal resolution and at daily temporal resolution.

Some CO_2 flux components are ignored in both these CHIMERE simulations and preliminary CIF-CHIMERE inversions: the biomass burning fluxes, and the fluxes associated to human/animal respiration, wood decomposition and lake/river outgassing. As stated above, these fluxes should be handled in a suitable way in the future series of reference inversions in D3.2.

3.3. Observations

All assimilated observations correspond to dry air mole fractions of CO_2.

3.3.1. Near-surface in-situ measurements

The inversion assimilates measurements of CO_2 mole fraction from the European Obspack compilation of atmospheric carbon dioxide data from ICOS and non-ICOS European ground based continuous measurement stations for the period 1972-2022 called “obspackco2466GLOBALVIEWplusv8.02023-03-30” (ICOS RI et al., 2023). ICOS-labelled stations have provided CO_2 data since 2015. The database also includes measurements from non-labelled sites for the full period of inversion. However, before 2015, the data coverage is relatively sparse (Figure 3.2). Following usual observation selection strategies (Broquet et al., 2013, Monteil et al., 2020) the inversion assimilates 1-hour averages of the measured CO_2 mole fractions during the time windows 12:00-18:00 UTC for low altitude stations (below 1000 masl) and 0:00-7:00 UTC for high altitude stations (above 1000 masl). When several levels of

This project has received funding from the European Union’s Horizon Europe research and innovation programme under grant agreement No 101081395

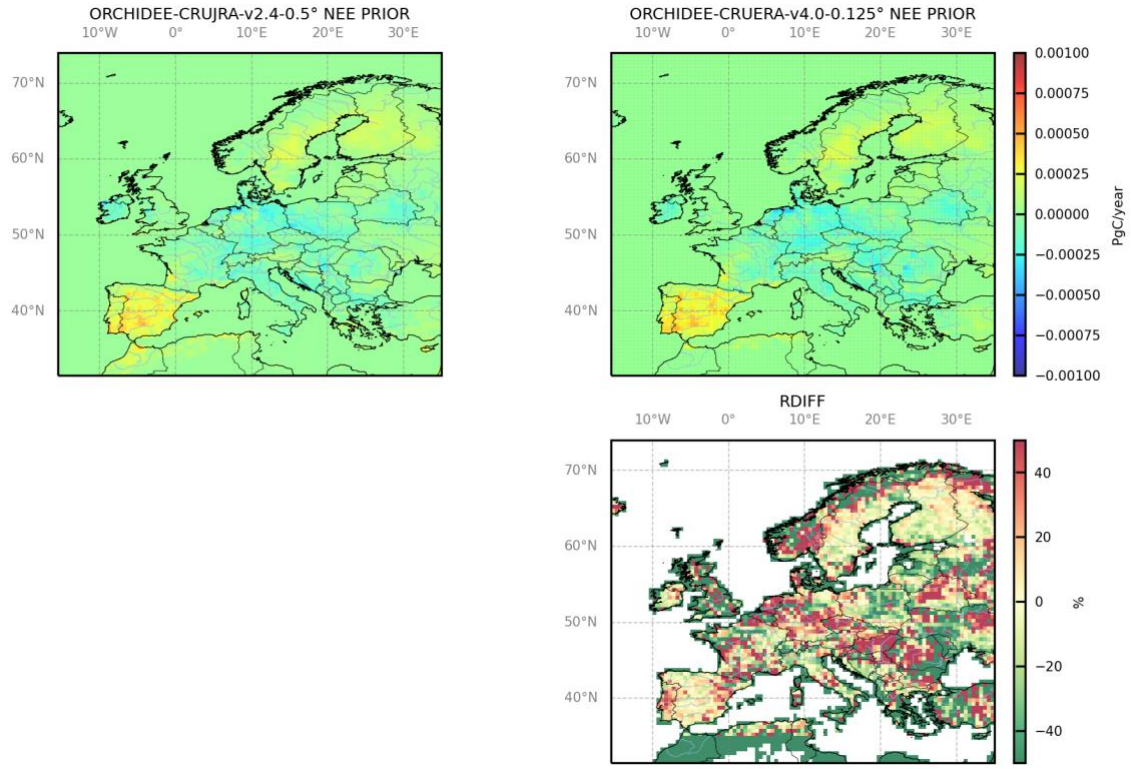

Figure 3.1: NBP annual gridded budgets from a) the CRUJRA and b) the CRUERA ORCHIDEE priors in PgC/year. c) Relative differences between the CRUJRA and the CRUERA ORCHIDEE priors in %, for 2005.

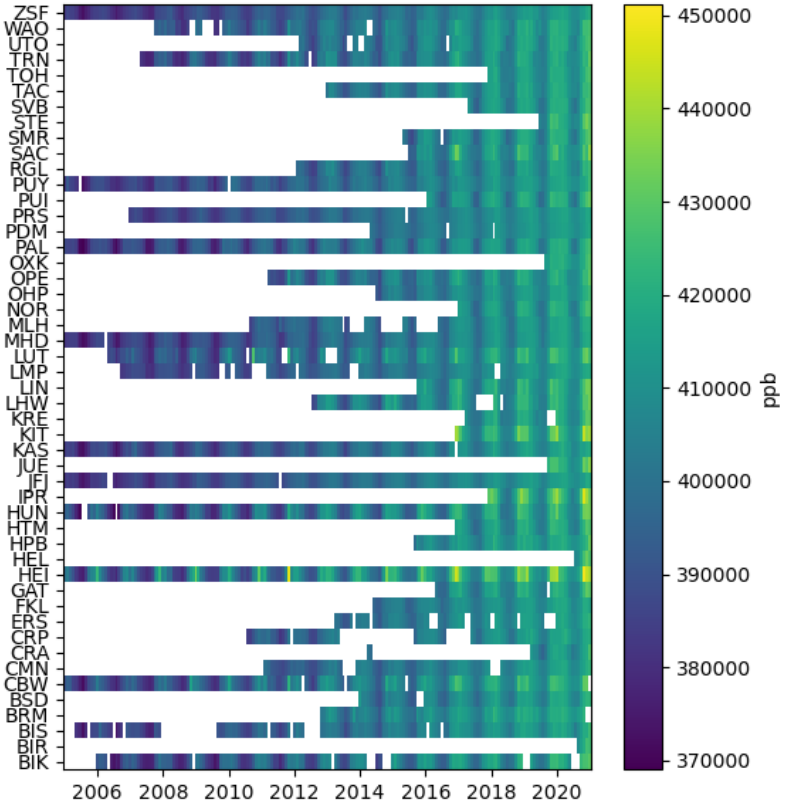

Figure 3.2: Observation temporal coverage at the different stations from 2005 to 2020: the months during which measurements are available at a given site are coloured. Blue to Yellow colour scale denotes monthly averaged CO_2 concentrations.

This project has received funding from the European Union's Horizon Europe research and innovation programme under grant agreement No 101081395

measurements are available at a given station, the inversions assimilate the data from the highest level only.

3.2.2. OCO-2 satellite observations

The inversion alternatively assimilates the relatively high-resolution satellite total column CO_2 mole fraction (XCO_2) observations from the OCO-2 NASA-JPL mission (the v11 dataset). The OCO-2 satellite carries high-resolution spectrometers that return high-precision measurements of reflected sunlight received within the CO_2 and O_2 bands in the short-wave infrared spectrum (Crisp et al., 2012) and flies on a 705 km sun-synchronous orbit with a 16-day (233 orbits) ground track repeat cycle. The nominal footprint of the OCO-2 ground pixels is 1.29 × 2.25 km^2 (across × along track) at nadir, with a cross-track swath width of about 10 km. We only consider "good" retrievals as identified by the XCO_2 quality flag of the product.

Although the biases in OCO-2 over the ocean acquired in glint mode have been substantially reduced since the initial version 7 (O'Dell et al., 2018), Chevallier et al. (2019) claimed that the assimilation of OCO-2 ocean observations still produced unrealistic results in their global atmospheric inversions. They are therefore not considered in this study. After this selection, all individual observations are assimilated and compared to their corresponding horizontal grid-cells in CHIMERE (i.e. to the CHIMERE CO_2 vertical column in this horizontal grid cell), defined for a given observation as that containing the centre of the ground projection of the OCO-2 pixel at the observation time: there is no aggregation of the observations at the model resolution. The average number of observations per month in the model 0.5° resolution grid cells in 2015 is shown in Figure 3.3., illustrating the higher coverage over Southern Europe than in Northern Europe during the whole period of observation.

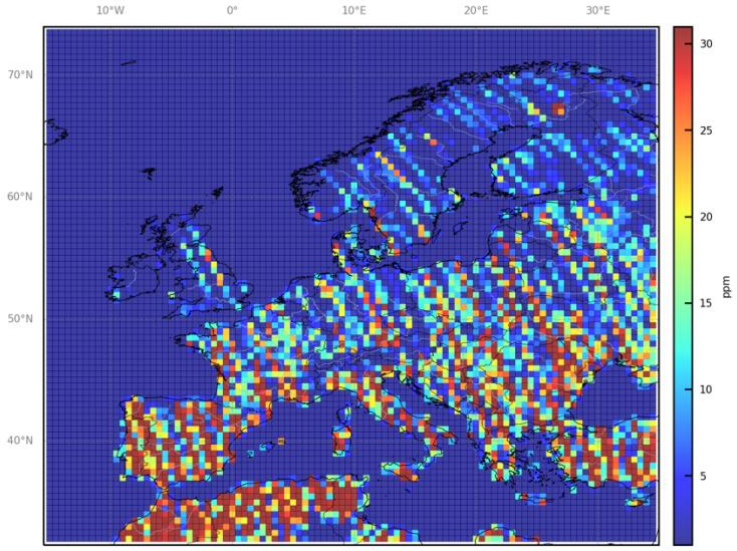

Figure 3.3: Average number of OCO-2 observations per month, in the model 0.5° resolution grid cells, in 2015.

As described in Section 3.1.2, the CAMS global CO_2 inversions are used to complement the vertical columns of CO_2 above the top boundary of CHIMERE when comparing the model to XCO_2 observations. To make suitable comparisons between simulations and satellite observations, the vertical profiles of CO_2 mole fraction in the corresponding atmospheric columns of the model simulations are first interpolated on the satellite CO_2 retrieval levels (with a vertical mass-conserving interpolation on pressure levels). Then, the appropriate simulated XCO_2 values are computed using both the OCO-2 averaging kernels and prior estimates provided in the OCO-2 retrieval product. As an example, the

This project has received funding from the European Union's Horizon Europe research and innovation programme under grant agreement No 101081395

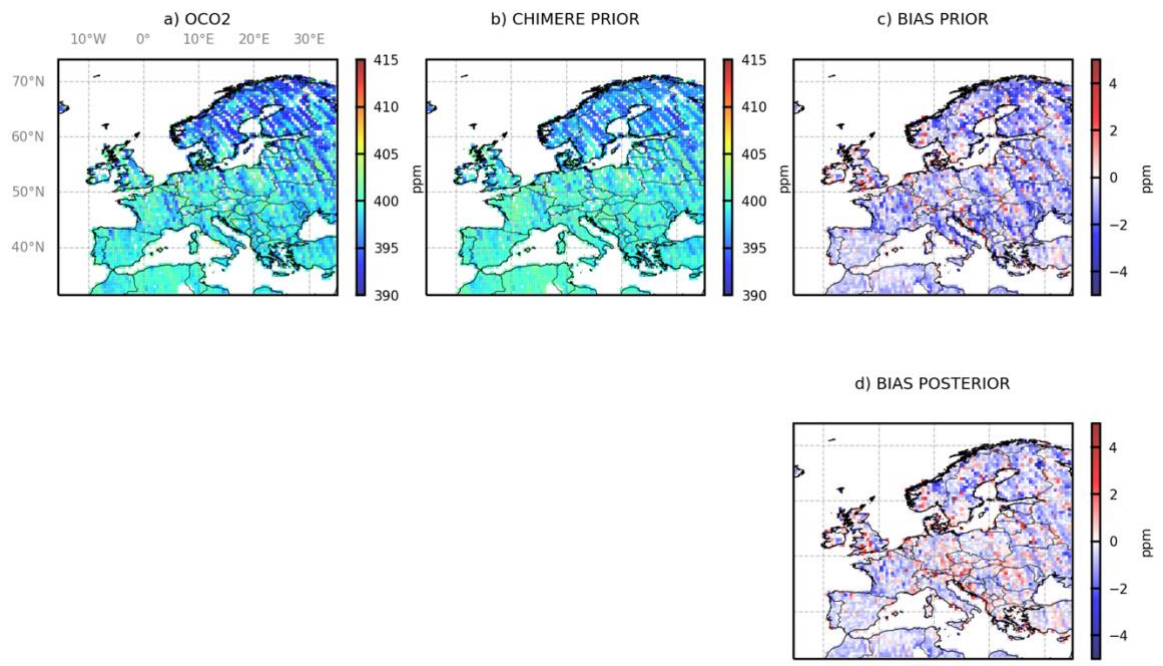

Figure 3.4: Comparison between the OCO-2 XCO_2 observations and the corresponding CHIMERE XCO2 simulations in 2015: averages over the year of the XCO_2 values per grid cell of the model (observations, prior and posterior simulations, and differences), in ppm.

average of the OCO-2 observations for the year 2015 is presented in Figure 3.4a while the average of the simulated XCO_2 values corresponding to these observations are presented in Figure 3.4b.

3.4. The inversion framework

The inversions of CO_2 NEE estimates consist in correcting the "prior" estimate of these fluxes (taken as the NBP from the ORCHIDEE simulations, see Section 3.1.3) to derive a “posterior” estimate with an improved fit between CHIMERE and the surface measurements of CO_2 mole fractions or XCO_2 satellite observations. Series of independent 13-month inversions have been performed to provide a posterior estimate of NEE since 2005 when using the surface measurements or since 2015 when using the satellite data. These 13-month inversions target individual years y, beginning on December 15th of the year y-1 and ending on January 15th of the year y+1 (to account for the lag-time between observations and the fluxes which impacted them, and for the temporal correlations of the prior uncertainties (see below), which connects observations at a given time to fluxes few weeks before or after), and we retain their results over the period January 1st to December 31st only when combining all results into time series of flux maps.

The inversion optimizes 6-hourly mean NEE fluxes at the 0.5°×0.5° resolution of CHIMERE. The uncertainty covariance matrix associated to the prior estimate of NEE is specified using the ORCHIDEE heterotrophic respiration, similarly to what is classically done in CO_2 inversions over Europe (Broquet et al., 2011; Monteil et al., 2020). Following the diagnostics of Kountouris et al. (2015), the temporal and spatial correlation scales for the uncertainty in the prior NEE (the prior uncertainty) are set to ≈1 month and 200 km, with no correlation between the four 6-hour windows of the same day. Different tests have been performed with or without controlling the model initial and lateral boundary conditions.

The observation error covariance matrix characterizing the transport model, CO_2 measurement and XCO_2 retrieval errors is set-up to be diagonal, ignoring the correlations between errors for different hourly averages of the CO_2 measurements (which has been justified by the analysis of Broquet et al., 2011), or between errors for different XCO_2 observations. The variance of the observation errors corresponding

This project has received funding from the European Union's Horizon Europe research and innovation programme under grant agreement No 101081395

to individual observations correspond to the Root Sum Square of the observation error values provided in the observation products and of values assigned to characterize the transport model error.

About 12 iterations are needed to reduce the norm of the gradient of the cost function *J* by 95% with the M1QN3 limited-memory quasi-Newton minimisation algorithm that we use (Gilbert and Lemaréchal, 1989).

3.4.1. Experiments

The different inversions performed in this study are presented in Table 3.1. Inversions using surface measurements without and with controlling the boundary conditions have been respectively performed for the period 2005-2019 and 2005-2022. The inversions using satellite observations have been conducted for the period 2015-2019.

3.5. Results

3.5.1. Fit to the assimilated observations

The reduction of the misfits between the simulation and the assimilated observations due to the corrections applied by the CIF-CHIMERE inversions to their prior estimate of the NEE is illustrated in Figure 3.4, in Figure 3.5 and in Table 3.2. Figure 3.5 presents time series of the monthly average of the CO_2 mole fractions for one low-altitude station (OPE, located in north-eastern France) and one high-altitude station (JFJ, located in Switzerland) over the year 2015. The two inversions "CRUJRA surface" and "CRUERA surface" lead to a similar improvement of the fit to the assimilated surface observations (Figure 3.5). As an illustration, when taking the hourly observations of all the stations into account, the reduction (from the prior to the posterior simulations) of the monthly RMS misfits between simulated versus measured hourly CO_2 during the assimilation windows is about 49%, 51% and 48%, respectively for the "CRUJRA surface", "CRUERA surface" and “CRUERA surface inibc” inversions, in July 2015 (Table 3.2). The reduction of the bias between simulated versus measured CO_2 reaches about 90%, 89% and 92% respectively, in July 2015 (Table 3.2).

Table 3.1: Description of the inversions performed in this study.

Name	Period	NEE Prior inventory	Observations	Control of the initial and lateral conditions
CRUJRA surface	2005-2019	ORCHIDEE CRUJRA	surface	No
CRUJRA OCO-2	2015-2019	ORCHIDEE CRUJRA	OCO-2	No
CRUERA surface	2005-2019	ORCHIDEE CRUERA	surface	No
CRUERA OCO-2	2015-2019	ORCHIDEE CRUERA	OCO-2	No
CRUERA surface inibc	2005-2022	ORCHIDEE CRUERA	surface	Yes

This project has received funding from the European Union's Horizon Europe research and innovation programme under grant agreement No 101081395

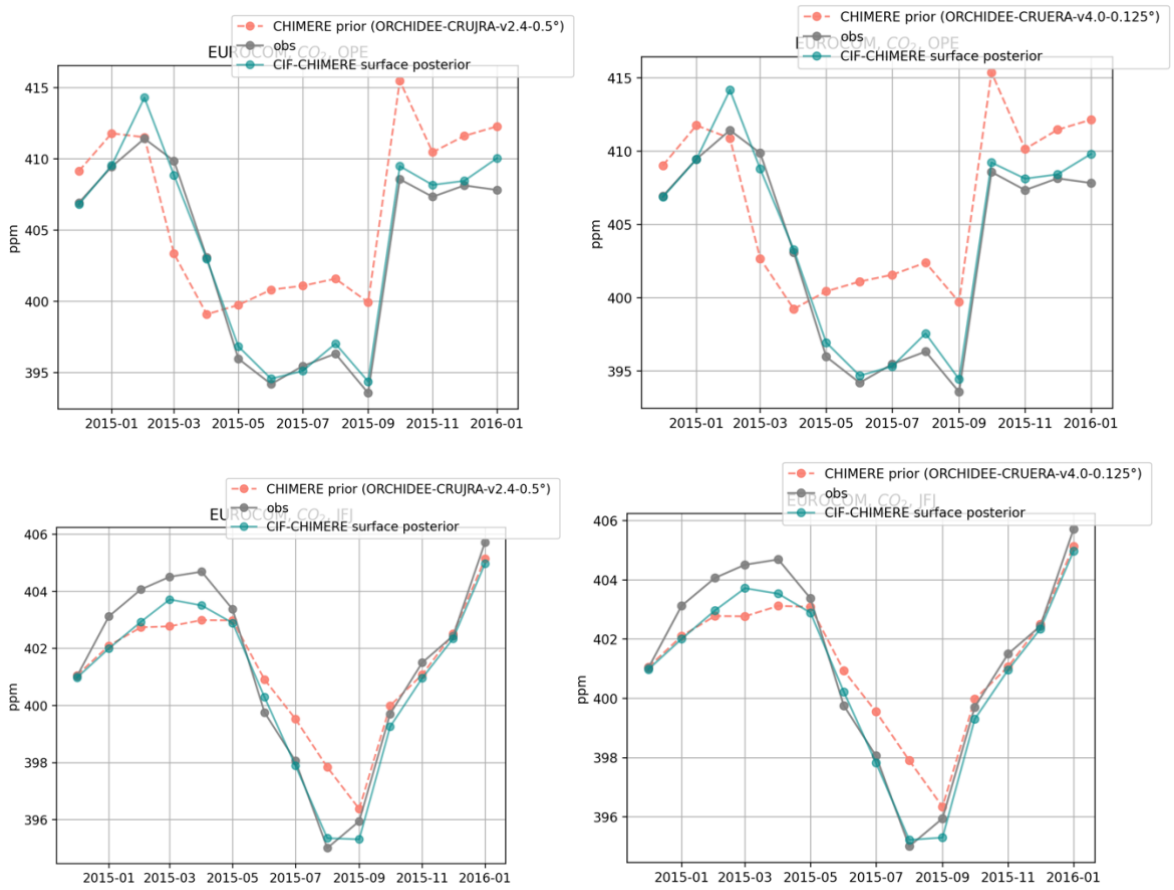

Figure 3.5: Time series of monthly averages of the CO_2 mole fraction corresponding the assimilated observations from one low-altitude station (OPE, top) and one high-altitude station (JFJ, bottom) over the year 2015: measurements (grey dots) and prior (green)/posterior (orange) simulations in the inversions assimilating surface data. The CHIMERE simulations and inversions use the ORCHIDEE CRUJRA (left) or the ORCHIDEE CRUERA NEE prior (right).

Table 3.2: Statistics on the performance of the CHIMERE CTM compared to assimilated mole fraction measurements, before and after the inversions. Mean prior, posterior and relative difference (RDiff) of determinant coefficient (R^2), Root mean squared error (RMSE) and bias, considering all the surface stations available in July 2015.

Inversion	**R^2**			**RMSE (ppm)**			**Bias (ppm)**		
	prior	**post**	**rdiff**	**prior**	**post**	**rdiff**	**prior**	**post**	**rdiff**
CRUJRA surface	0.37	0.55	0.48	6.12	3.02	-0.49	4.29	0.41	-0.90
CRUERA surface	0.38	0.52	0.36	6.19	3.18	-0.51	4.54	0.5	-0.89
CRUERA surface inibc	0.38	0.55	0.44	6.19	2.99	-0.48	4.54	0.35	-0.92

This project has received funding from the European Union's Horizon Europe research and innovation programme under grant agreement No 101081395

3.5.2. Spatial variability of the annual corrections applied to the prior terrestrial ecosystem fluxes from surface and OCO-2 observations

Figure 3.6. presents maps of the annual corrections provided by the inversions to the ORCHIDEE CRUERA prior estimates when assimilating surface and OCO-2 observations from 2015 to 2019. A common pattern from the inversions assimilating surface observations is positive corrections over Switzerland, southern Germany and over Poland. The positive increments over Switzerland, and southern Germany seem to be mainly due the underestimation of the CO_2 mole fractions in the prior CHIMERE simulations compared to the surface measurements at the BRM station in winter and spring. The inversions using OCO-2 satellite data as observations only present annual negative correction to the prior estimates.

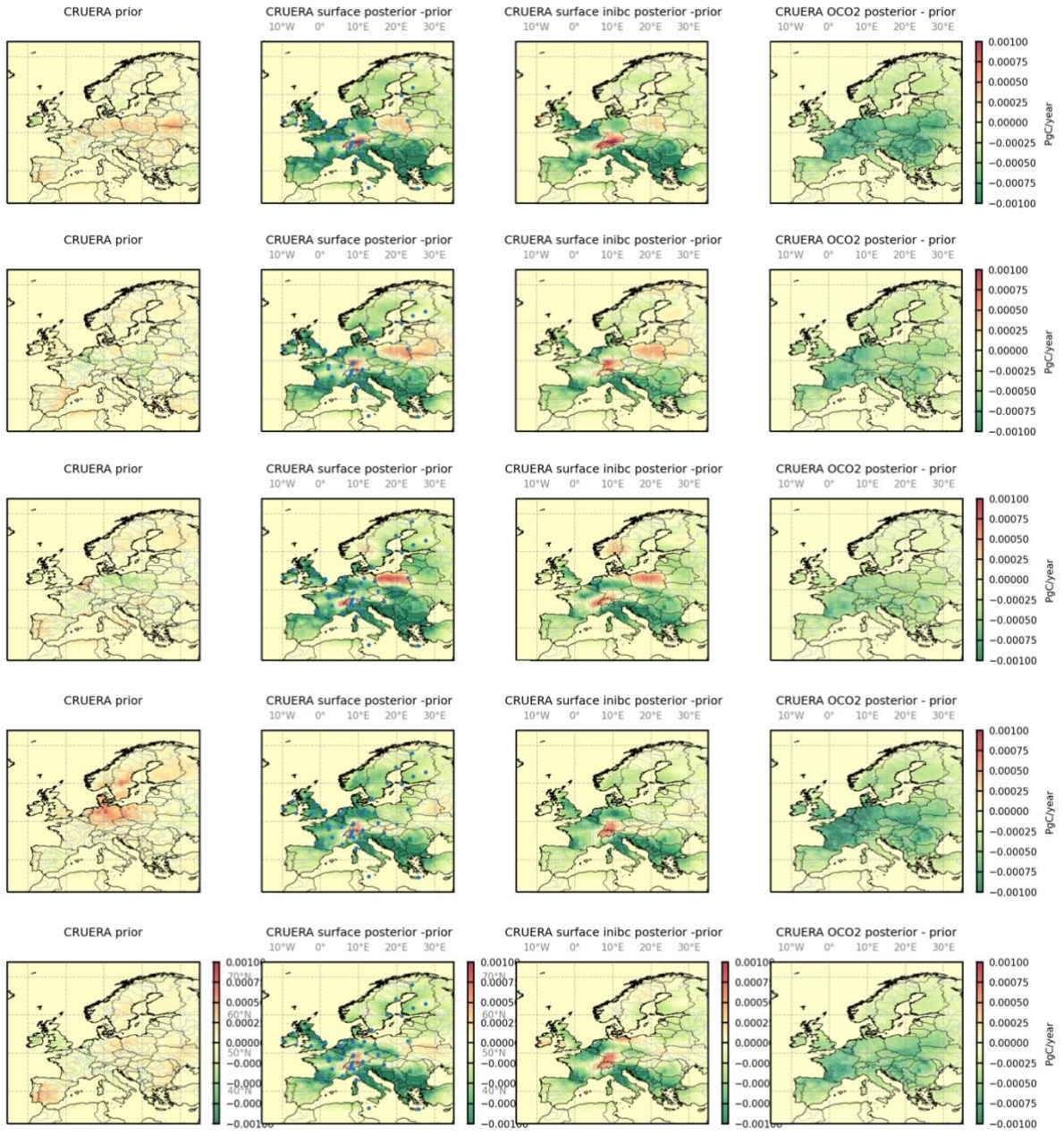

Figure 3.6: Maps of the ORCHIDEE CRUERA prior estimates and of the annual corrections provided by the inversions to these priors when assimilating surface or OCO-2 observations, in PgC/year, from 2015 (top) to 2019 (bottom).

This project has received funding from the European Union's Horizon Europe research and innovation programme under grant agreement No 101081395

3.5.3. Seasonal cycle of the EU27+UK NEE budget

Figure 3.7 presents times series of monthly estimates of the CO_2 NEE from prior and posterior estimates from surface and satellite observations, from January 2015 to December 2019 for the European Union (EU27) + UK area. In terms of magnitude of the fluxes, all the inversions increase the CO_2 uptake in spring and contrarily decrease the CO_2 emissions in autumn and winter compared to the ORCHIDEE prior estimates.

Similar seasonal cycles are obtained from the different inversions, all of which shift the CO_2 maximum to later in the year compared with the ORCHIDEE priors. The priors both present a CO_2 positive maximum in October (excepted in 2015 where the positive maximum occurs in November) while the posterior estimates from surface inversions indeed rather often show the CO_2 positive maximum in November (even in December in 2017). A similar 1-month gap is generally found with the inversions assimilating satellite data (Figure 3.7).

The prior and the posterior estimates from the OCO-2 observations agree for identifying the CO_2 peak uptake in May (excepted in 2015 where the peak uptake occurs in April for the ORCHIDEE prior). This timing is not confirmed by the surface inversions, showing the CO_2 peak uptake in June (Figure 3.7).

The NEE alternates between being a neutral flux and a positive net CO_2 source between July and February in the ORCHIDEE priors while the corresponding period often occurs between September and February/March in the posterior estimates from surface and OCO-2 inversions. This high positive NEE found by ORCHIDEE at the end of the summer (>0.10 PgC per month in August and September) was already contradicted in Monteil et al. (2020), the median of the ensemble of inversions from their study estimating the NEE at ≈0.04 Pg C per month in these two months. In our estimates from surface and OCO-2 inversions, the NEE is often >-0.10 PgC for these two months.

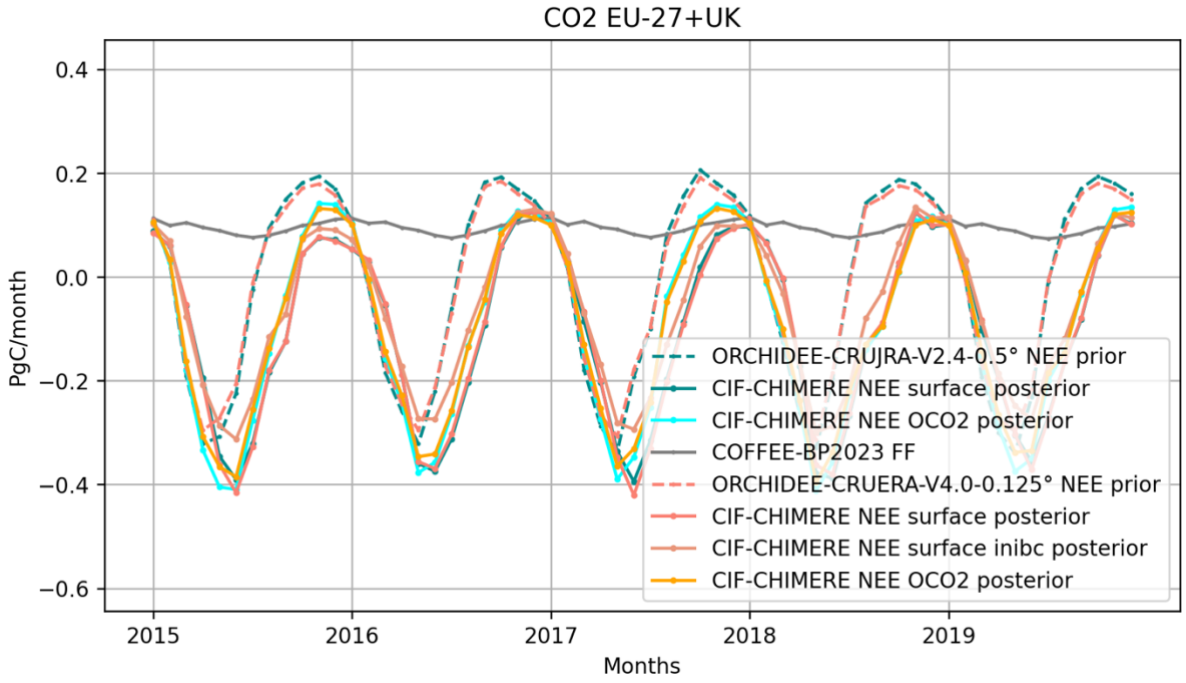

Figure 3.7: Times series of monthly estimates of the CO2 NEE, in PgC/month, from January 2015 to December 2019, for the EU-27+UK area. Dashed green and orange lines are respectively for the CRUJRA and CRUERA priors while solid lines are for posterior estimates.

This project has received funding from the European Union's Horizon Europe research and innovation programme under grant agreement No 101081395

3.5.4. Long-term mean of the annual EU27+UK NEE budget

From prior estimations of about -0.2 PgC.yr^{-1}, the posterior estimates of the NEE average annual budget for EU27+UK over the period 2005-2019 from the surface inversions without controlling boundary conditions is of about -0.90 PgC.yr^{-1}. We find posterior estimates of the NEE average annual budget for EU27+UK over the period 2006-2015 of about -0.82 PgC.yr^{-1} and -0.78 PgC.yr^{-1}, respectively, for the "CRUJRA surface" and the "CRUERA surface" inversions. Our system therefore finds the European ecosystems to be on average a sink of CO_2 to the atmosphere over our simulation period, consistently with recent studies (Monteil et al., 2020; Chevallier, 2021; Petrescu et al., 2021; Munassar et al., 2022; McGrath et al., 2023).

These estimates are not exactly comparable with the estimates of Petrescu et al. (2021) and McGrath et al., (2023), subtracting the emissions from inland waters (rivers, lakes and reservoirs) and, in the second case, emissions due to crop and wood consumption, from the inversion results. However, the net sinks of -0.82 PgC.yr^{-1} and -0.78 PgC.yr^{-1} for the EU27+UK area found from surface inversions without controlling boundary conditions for the period 2006-2015 are strongly higher than the ones estimated respectively by the EUROCOM (annual mean of -0.13 PgC) and by the CarboscopeReg (annual mean of -0.38 PgC) ensembles of inversions in Petrescu et al. (2021). Our surface inversion estimates also show a trend towards more negative fluxes between 2010 and 2015 (Figure 3.8), which is not seen in other inversion results (e.g., from the EUROCOM-v2020 and GCP-v2021 ensembles in McGrath et al., 2023). Then, the sink no longer increases and even slightly decrease between 2015 and 2019 at the EU-27+UK scale (Figure 3.8), similarly with the global inversions using surface measurements of Chevallier et al. (2021).

The large range of variability of inversion results in previous studies (e.g., in the EUROCOM ensemble estimates in Monteil et al. (2020) demonstrates that there is still a very significant uncertainty in the estimates from surface inversions. The variability seen from the inversion estimates can be explained by uncertainties inherent to the limitations of the observation network, especially before 2006. It is however interesting to note that satellite observations provide estimates of the CO_2 sink relatively consistent with the estimates from our surface-observation inversions (Figure 3.8).

This variability seen from the inversion estimates can also be explained by uncertainties in the atmospheric transport modeling and boundary conditions (Petrescu et al., 2021; McGrath et al., 2023). Our results between 2015 and 2019, from surface inversions that do not control the boundary conditions, showing a decrease of the CO_2 NEE sink similarly with the global inversions from surface measurements of Chevallier et al. (2021) used here for the generation of the initial, lateral and top conditions for CO_2 concentrations, indeed suggest that these boundary conditions could be responsible for the trend in our inversions. Preliminary tests with inversions controlling the boundary conditions seem to confirm their strong impact on the annual NEE budgets (Figure 3.8): these boundary conditions should be controlled in the future series of inversions in D3.2 due in M28.

Other additional analyses are also needed to examine the factors controlling the CO_2 NEE budgets (e.g., impact of the resolution, impact of the prior fluxes, impact of the prescribed anthropogenic emissions). In this context, inversions at the relatively high-resolution of 0.2° are performed and analyzed in D3.3.

This project has received funding from the European Union's Horizon Europe research and innovation programme under grant agreement No 101081395

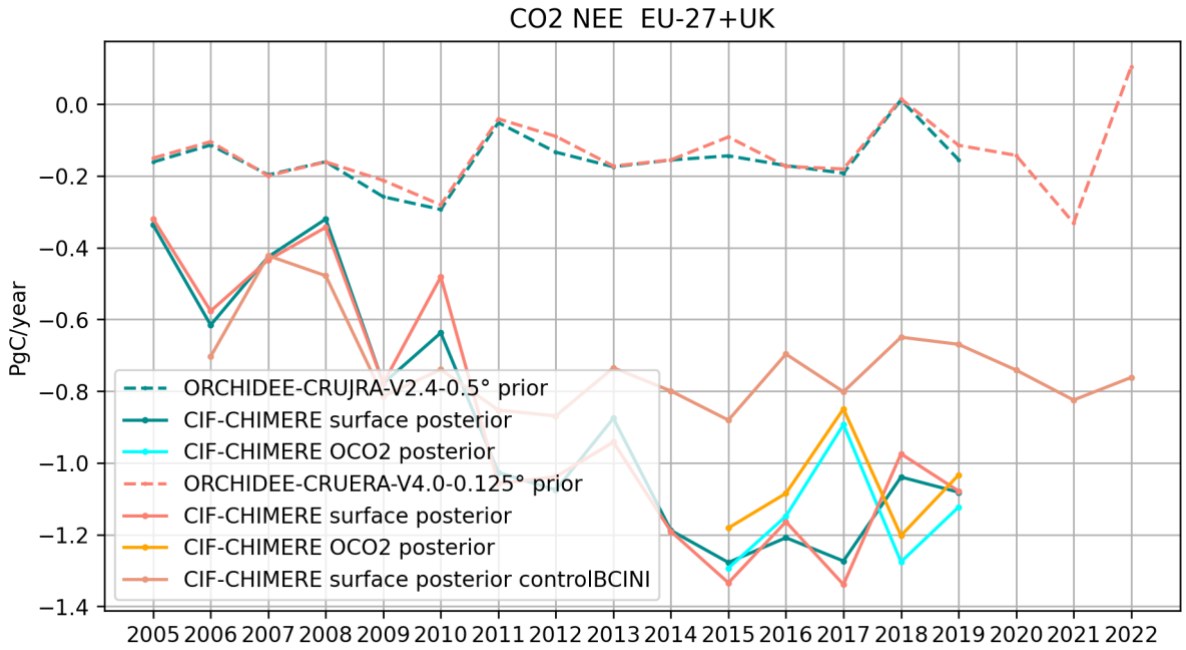

Figure 3.8: Times series of annual prior and posterior estimates of the CO_2 from the surface inversion, in PgC/year, from 2005 to December 2022 for the EU27+UK area.

4. CH_4 inversions

For this first deliverable, we used the atmospheric inversion model CarbonTracker Europe - CH_4 (CTE-CH_4) (Tsuruta et al. 2017) to estimate methane (CH_4) emissions in Europe. The test was carried out with an established system, because the implementation of TM5-MP to the CIF system was still under development. In addition, we wanted to test how the use of CIF instead of CarbonTracker Europe - CH_4, which uses CTDAS (van der Laan-Luijkx et al. 2017), affects the inversion model results, meaning we need to have results from both systems using, for example, the same priors. Thus, a test with CTE-CH_4 was found to be justified. The inversion run extended from 2016 until the end of 2021.

4.1. Inversion settings

In this task, we used the global atmospheric inversion model CTE-CH_4 to estimate CH_4 emissions at a 1°×1° resolution over the high northern latitudes and at a weekly temporal resolution using in situ measurements of atmospheric CH_4 concentrations. The system consists of prior flux maps for different emission sources, the atmospheric chemistry transport model TM5 (Krol et al. 2005), and an ensemble Kalman filter data assimilation scheme (Peters et al. 2005) with an ensemble size of 500 and a 5-week lag. TM5 is run at a global horizontal resolution of 4°×6° (latitude × longitude) with a 1°×1° zoom and a 2°×3° intermediate zoom around the 1°×1° zoom grid over Europe (see Tsuruta et al. 2019). TM5 is driven by 3-hourly ECMWF ERA5 meteorological data (Hersbach et al. 2020). Vertically, TM5 has 25 hybrid sigma pressure levels from the surface to the top of the atmosphere. The monthly atmospheric sink due to photochemical reactions with OH is based on Houweling et al. (2014) and Cl and O(1D) are based on the atmospheric chemistry general circulation model ECHAM5/MESSy1 (Joeckei et al. 2006, Kangasaho et al. 2022). The inversion model did not account for annual variations in atmospheric sinks and did not optimise atmospheric sinks.

We simultaneously optimised anthropogenic and natural fluxes at a resolution of 1°×1° over Canada, the USA, Europe and Russia, and regionally elsewhere (see e.g. Tenkanen et al. 2023). The prior

This project has received funding from the European Union's Horizon Europe research and innovation programme under grant agreement No 101081395

uncertainties for the anthropogenic and natural fluxes were set to 80% for land fluxes and 20% for ocean fluxes and assumed to be uncorrelated. Our covariance matrix **B** is computed as $\mathbf{B}=\mathbf{D}^T\cdot\mathbf{C}\cdot\mathbf{D}$ (Meirink et al., 2008) where the diagonal flux uncertainty **D** assumed to be 80% of the prior flux over land and 20% over ocean and **C** is a non-diagonal element that declines exponentially with distance **x** between grid cells as $\exp(-x^2/l^2)$. The observational uncertainties **R** encompass both measurement uncertainty and the error in modeling the mixing ratios and ranged from 4.5 to 75 ppb for global sites and from 15 to 75 ppb for European sites. The spatial correlation was defined by an exponential decay (Peters et al. 2005), with a correlation length of 100 km between the 1°×1° grid-based optimisation domains, 500 km over other land domains and 900 km over ocean domains.

4.2 Prior fluxes

We used the same prior CH_4 emissions as was used in CIF-FLEXPART CH_4 inversions at 0.2° (D3.3). Monthly data were used for anthropogenic, biospheric and fire prior emissions, and climatological values were used for oceanic, geological and termite prior emissions. For anthropogenic emissions, a combination of GAINS (from WP2) and EDAGR v8 was used. GAINS covered the EU27 countries along with the UK, Norway and Switzerland. Emissions from regions not covered by GAINS were taken from EDGAR v8. As biospheric prior emissions, estimates from JSBACH-HIMMELI (WP2) were used. Similar to anthropogenic emissions, JSBACH-HIMMELI only covered the European domain, so its estimates were combined with estimates from another process-based model, LPX-Bern DYPTOP v1.4 (Lienert et al. 2018, Saunois et al. 2024). These biosphere emissions aggregate emissions from peat, inundated soils and net mineral soil emissions. Emission estimates for fire emissions were obtained from GFEDv4.1s (van der Werf et al. 2017), excluding agricultural waste burning emissions as these were already included in our anthropogenic prior emissions. For ocean emissions, we used climatological estimates from Weber et al. (2019). Geological emissions were taken from Etiope et al. (2019) and downscaled globally to 23 Tg (best value estimated by IPCC AR6 WG1 report), following the inversion model protocol of the Global Methane Budget (Saunois et al. 2024). Finally, emissions from termites were based on the results of Saunois et al. (2020). All prior emissions were converted to the 1°×1° resolution.

4.3 Observations

We used observations from a global in situ measurement network, including the ICOS dataset, NOAA GLOBALVIEWplus ObsPack v4.0 dataset (Shuldt et al. 2021) and observations from the National Institute for Environmental Studies (JR-STATION: Japan-Russia Siberian Tall Tower Inland Observation Network, Ver1.2 (Sasakawa et al. 2010)) and the Finnish Meteorological Institute (Tsuruta et al. 2019). The data included weekly discrete air samples as well as hourly continuous measurements. The data were filtered according to the quality flags of the data providers. Only data points representing well-mixed conditions were used: the hourly continuous observations were preprocessed to daily averages by averaging from 12 to 4 pm local time, except for the high mountain sites, from which averages were taken from 0 to 4 am local time, similar to Tsuruta et al. (2017). Observational uncertainty, also known as model-data mismatch, was defined for each site based on site characteristics and measurement accuracy adapted from previous studies (Tsuruta et al. 2017, 2019, Bruhwiler et al. 2014) and also reflected the ability of the model to predict atmospheric concentrations. In the European domain, there were 34 sites (observations in Fig. 4.1 and locations in Fig. 4.2) and globally 126 stations in 2016-2021. Some sites had both continuous and discontinuous measurements.

This project has received funding from the European Union's Horizon Europe research and innovation programme under grant agreement No 101081395

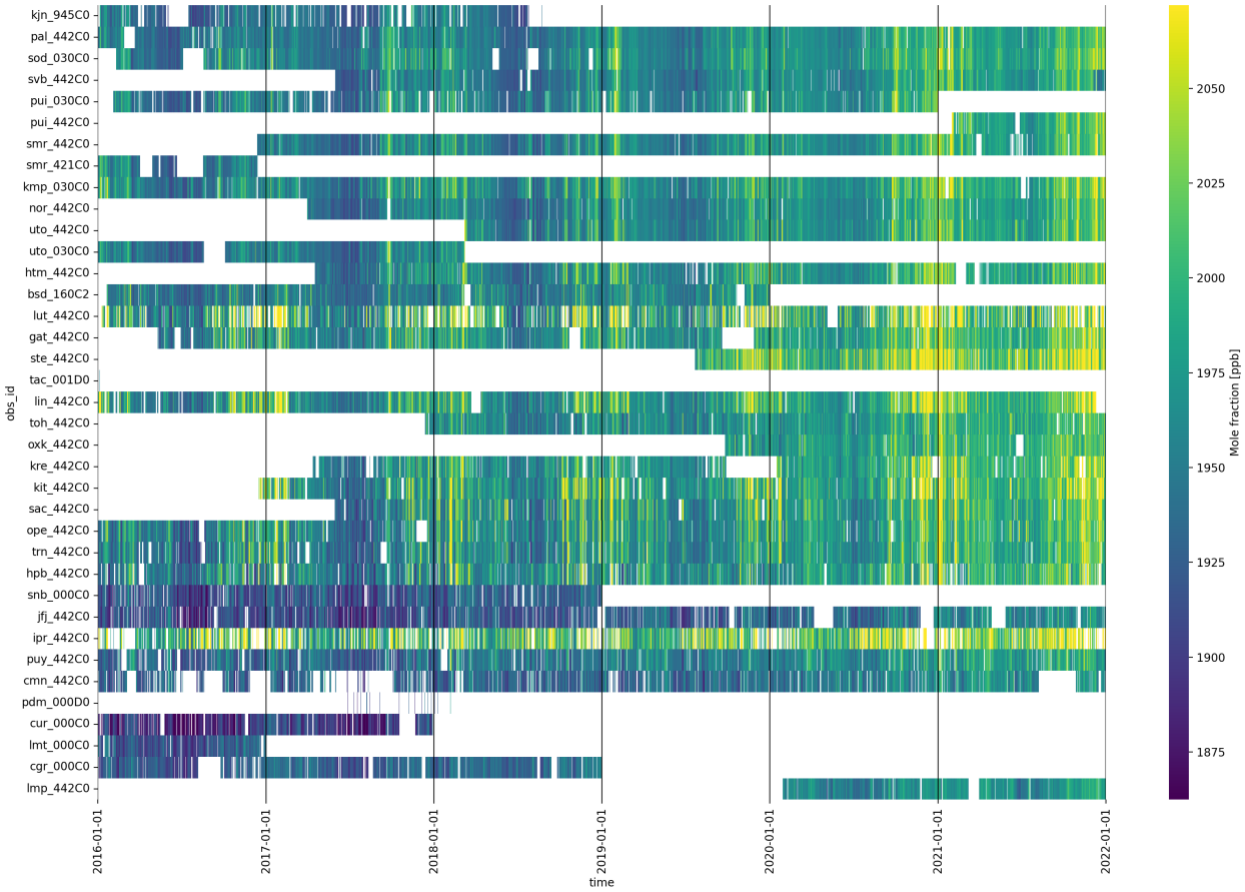

Figure 4.1: Daily averaged CH_4 mole fraction observations (ppb) in European measurement stations in 2016-2019. The stations are ordered by their latitudes, the northernmost at the top and the southernmost at the bottom).

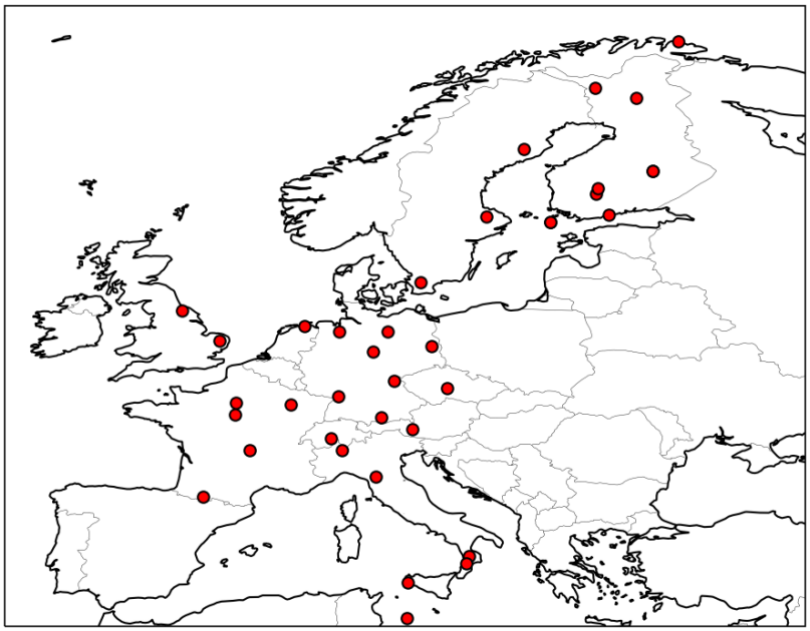

Figure 4.2: Geographical distribution of sites used in the data assimilation.

This project has received funding from the European Union's Horizon Europe research and innovation programme under grant agreement No 101081395

4.4. Results

Here, we discuss the results from the European domain. The domain boundary was defined to align with the estimates from JSBACH-HIMMELI: longitude ranging from 12°W to 37°E and latitude ranging from 35°N to 73°N.

4.4.1 Comparison of modelled and observed atmospheric CH_4 mole fractions

We compared the observed CH_4 mole fractions used in the inversion with the modelled mole fractions before (prior) and after (posterior) the optimisation. We calculated the linear correlation coefficient (R), coefficient of determination (R^2), root mean square error (RMSE) and bias between the observation and modelled values. The statistics for each European site are shown in Fig. 4.3 and averages in Table 4.1. As seen from the figure and the table, the agreement before the optimisation varied between the sites but after the optimisation, the agreement between the observed and modelled mole fractions were good.

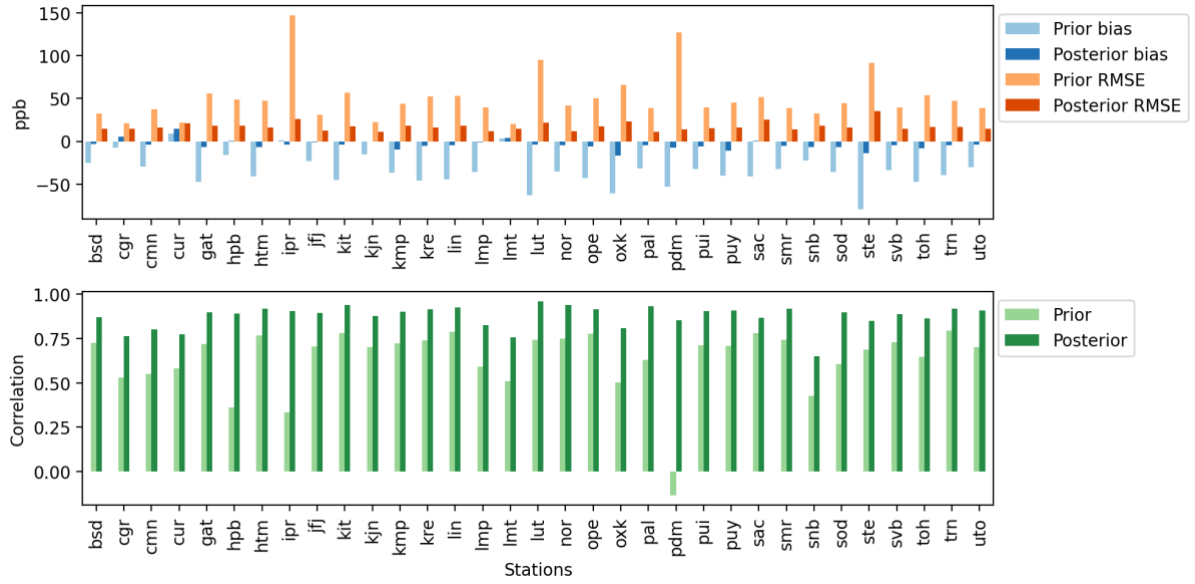

Figure 4.3: Overview of statistical results for assimilated observed mole fractions and CTE-CH_4 posterior and prior simulated concentrations from all stations used in the inversion: RMSE and bias (upper panel), and correlation (lower panel).

Table 4.1: Statistics on the performance of the CTE-CH_4 compared to assimilated mole fraction measurements, before (prior) and after (post) the inversions. Mean prior, posterior and relative difference (RDiff) of coefficient of determination (R^2), Root mean squared error (RMSE) and bias, considering all the surface stations used.

Inversion	**R^2**			**RMSE (ppb)**			**Bias (ppb)**		
	prior	**post**	**rdiff**	**prior**	**post**	**rdiff**	**prior**	**post**	**rdiff**
CTE-CH_4 surface	0.43	0.77	0.76	50.69	17.24	-0.66	-33.09	-4.20	-0.88

4.4.2 Spatial distribution of prior and posterior emissions

Figure 4.4 shows the average annual biospheric, anthropogenic and total CH_4 emissions from 2016-2021 at 1°×1° resolution. The sum of the other emissions (fire, ocean, geological and termites) are

This project has received funding from the European Union's Horizon Europe research and innovation programme under grant agreement No 101081395

shown in Fig. 4.5 (plots of the prior emissions by source type are shown in the deliverable D3.3). Prior and posterior emissions are shown as well as their difference (posterior minus prior). Most of the biospheric CH_4 emissions were estimated to occur in northern Europe, Ireland, the UK and Italy. The inversion increased biospheric emissions most in northern Finland. Elsewhere the changes were smaller.

Anthropogenic CH_4 emissions were mostly concentrated in Western and Southern Europe, with several hotspots in Germany, the Netherlands, the UK and France, and single hotspots in Poland and Italy. The inversion mostly increased emissions in the areas with the highest sources, except in Italy where emissions decreased. Italy had high geological emissions, which were not optimised. The increase was especially prominent in the Netherlands, Germany, France, the UK, Poland and the Czech Republic.

As anthropogenic emissions were about ten times higher than biospheric emissions in the European domain, the spatial distribution of total CH_4 emissions follows that of anthropogenic emissions.

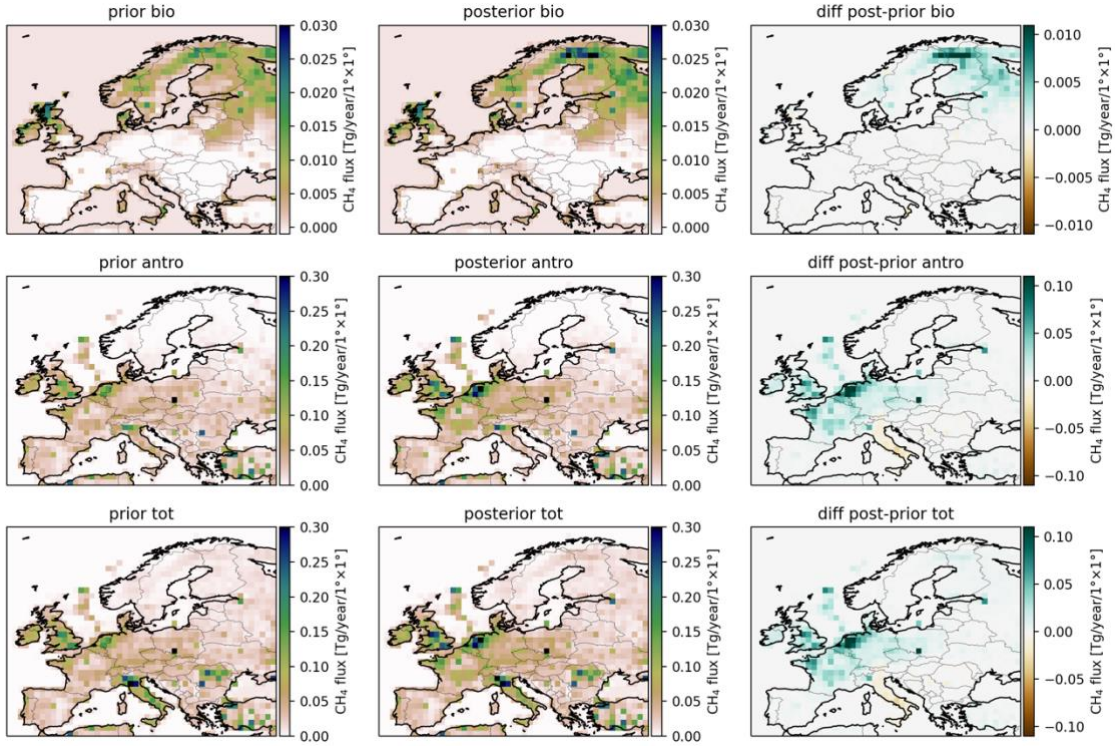

Figure 4.4: Annual average CH_4 estimates from CTE-CH_4 inversion at the resolution of 1°×1° from 2016-2021: prior (left panel), posterior (middle panel) and posterior increments computed as (posterior – prior) (right panel). The top row shows the biospheric, the middle anthropogenic and the bottom the total CH_4 emission estimates. Note that biospheric CH_4 emission figures have colour bars with different ranges than the rest of the figures.

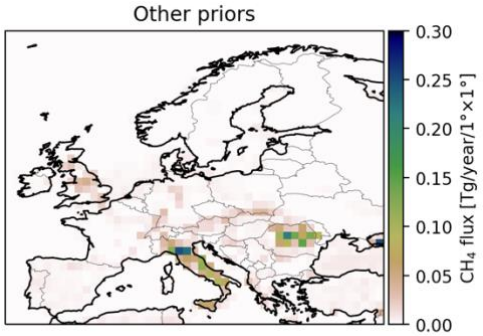

Figure 4.5: Annual average CH_4 estimates of fire, ocean, geological and termites from 2016-2021.

This project has received funding from the European Union's Horizon Europe research and innovation programme under grant agreement No 101081395

4.4.3 Annual and monthly emission estimates

The timeseries of the annual CH_4 emissions in the EU27 including the UK, Norway and Switzerland are shown in Fig. 4.6. Both the biospheric and anthropogenic prior and posterior emissions are shown along with the total emissions. The ten-fold difference between the biospheric and anthropogenic emissions is evident, though, the inversion increased both the biospheric and anthropogenic CH_4 emissions. The average annual biospheric emissions (JSBACH (WP2)) were 1.32 Tg/yr (in Tg(CH_4) here and hereafter) while the posterior emissions were 1.52 Tg/yr. The anthropogenic prior emissions (GAINS (WP2)) were 15.00 Tg/yr and the posterior emissions were 19.92 Tg/yr. The total CH_4 emissions were increased from 20.82 Tg/yr to 25.94 Tg/yr. Fire, ocean, geological and termites CH_4 emissions were together 4.5 Tg/yr.

The GAINS (WP2) emission estimates decreased slightly from 2016 to 2021 but the inversion increased the emissions especially in 2020 and 2021 so that the posterior anthropogenic emissions were larger in 2021 than in 2016. In addition, the increase from the biospheric prior to posterior emissions were relatively high in 2020 and in 2021.

Figure 4.7 shows the monthly CH_4 emissions from the same region. The optimisation increased the amplitude of the seasonal cycle for both biospheric and anthropogenic CH_4 emissions. In the anthropogenic prior there was no clear maximum, but in the anthropogenic posterior the maximum was found to be in August. The minimum was consistent between the prior and posterior emissions, although there was more variability in the posterior emissions.

Biospheric CH_4 emissions showed a clear seasonal cycle. The minimum of prior and posterior emissions was in good agreement, with emissions close to zero during the winter months. The maximum was shifted one or two months later: in the prior (JSBACH (WP2)) the maximum was in July or June, but in the posterior the maximum was in August or July. In addition, emissions in spring were decreased compared to the prior, but emissions in late summer and autumn were increased.

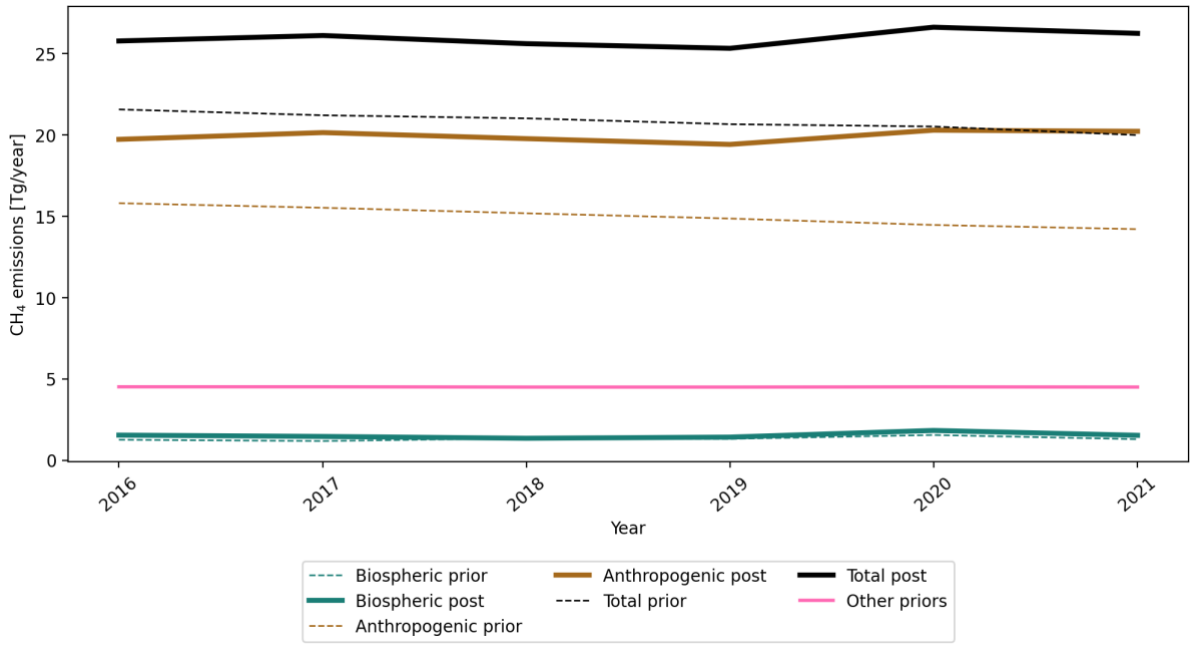

Figure 4.6: Times series of annual estimates of CH_4, in Tg(CH_4)/yr, from 2016 to 2021, for the EU-27+UK+Norway+Switerland area. Prior (dashed lines) and optimised (solid lines) CH_4 emissions are shown for biospheric, anthropogenic and total CH_4. Emissions of other sources (fire, oceanic, geological and termite) which were taken as their priors, are shown with the pink line.

This project has received funding from the European Union's Horizon Europe research and innovation programme under grant agreement No 101081395

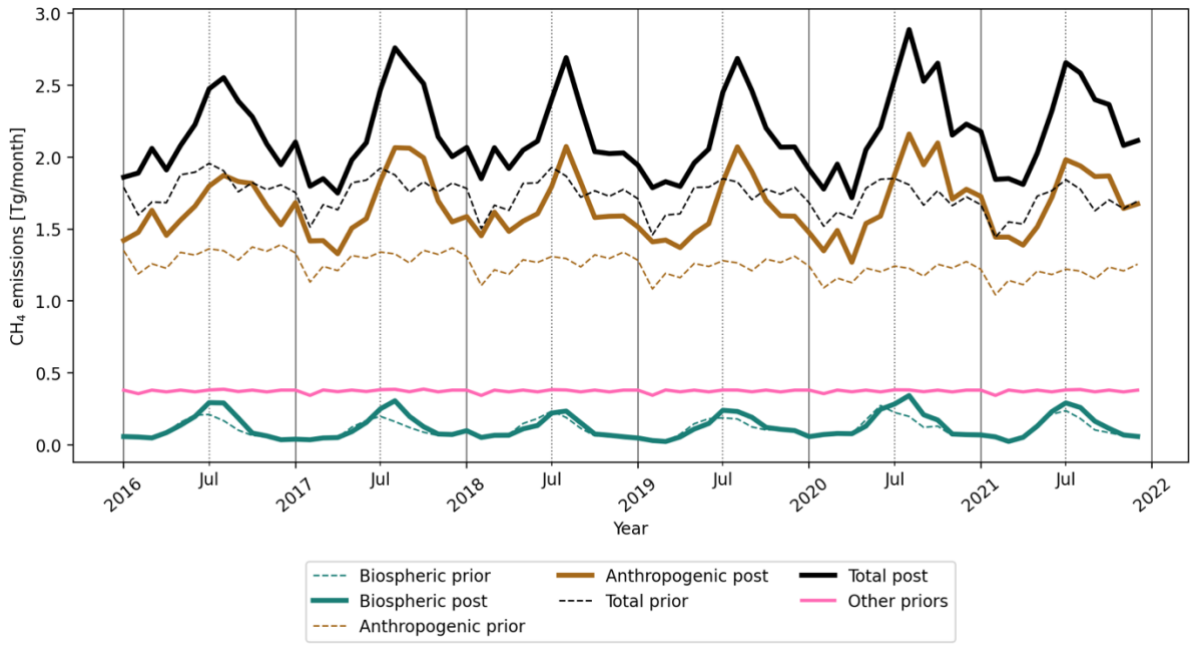

Figure 4.7: Times series of monthly estimates of CH_4, in Tg(CH_4)/month, from January 2016 to December 2021, for the EU-27+UK+Norway+Switerland area. Prior (dashed lines) and optimised (solid lines) CH_4 emissions are shown for biospheric, anthropogenic and total CH_4. Emissions of other sources (fire, oceanic, geological and termite) which were taken as their priors, are shown with the pink line.

5. N_2O inversions

This section describes the CIF-FLEXPART configuration for N_2O inversions over Europe.

5.1 Inversion framework and transport model

In this task, we used the Community Inversion Framework combined with the Lagrangian particle dispersion model, FLEXPART v11 (CIF-FLEXPART) to estimate N_2O emissions at a 0.5° × 0.5° resolution over the Europe using ground-based measurements of atmospheric N_2O mole fractions. N_2O emissions are estimated in this deliverable for the period from 2015 to 2020.

Since in Lagrangian models the transport computations can be reversed in time, this allows the Jacobian matrix describing the relationship between the change in an observed mixing ratio to the fluxes to be derived – the so-called source-receptor relationship (SRR). As such, Lagrangian models are said to be self-adjoint. The CIF is coupled to the SRRs calculated by prior runs of FLEXPART, which allow both mixing ratios to be simulated as well as the inversion to be performed. The FLEXPART SRRs are calculated globally with a horizontal resolution of 2°×2° and for a nested domain at 0.5°×0.5° resolution over Europe. FLEXPART is driven using hourly ECMWF ERA5 meteorological data at 0.5°×0.5° resolution.

The prior uncertainties were set to 50%. The spatial correlation was defined with a correlation length of 200 km over other land domains and 1000 km over ocean domains.

A variable-resolution grid was defined for the inversion as shown in Fig. 5.1, which is based on the total SRRs, and coarser resolution is used where there is little information provided by the observations about the fluxes. The grid cells in the domain correspond to 2°, 1° and 0.5° resolution. Using an aggregated grid has the advantage of reducing the dimension of the inversion problem, thus reducing the computation time and memory required, while avoiding introducing aggregation error.

This project has received funding from the European Union's Horizon Europe research and innovation programme under grant agreement No 101081395

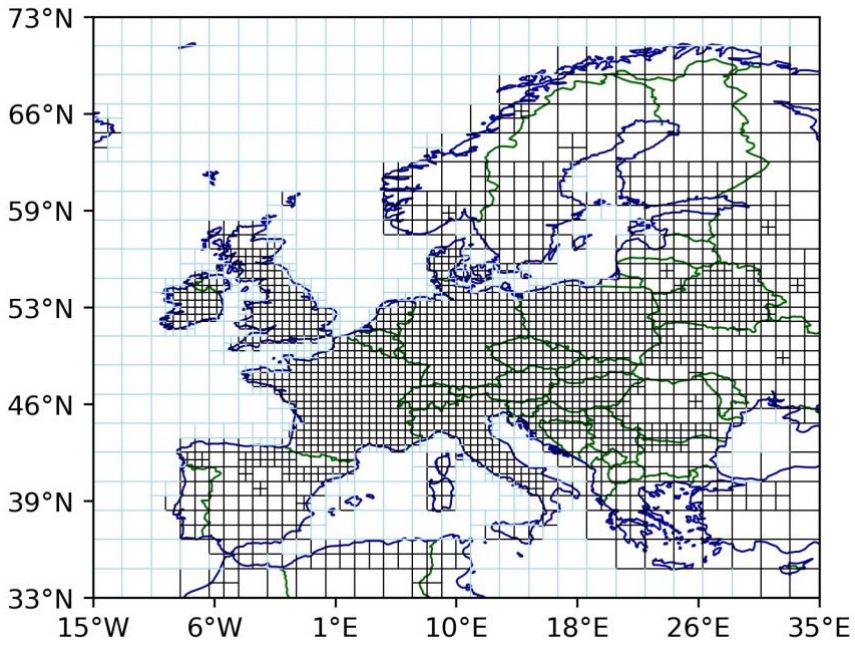

Figure 5.1: Variable-resolution grid used in the inversion

5.1 Prior Fluxes

To generate comprehensive N_2O emission estimates, we incorporate monthly data from major source categories: agriculture, other anthropogenic emissions, biomass burning, natural soils, as well as climatological estimates for ocean emissions. Our monthly prior flux data for agriculture and other anthropogenic emissions is sourced from GAINS (from WP2) for EU27 plus United Kingdom, Norway, and Switzerland (EU27+3). Agriculture emissions include livestock and indirect emissions. Other anthropogenic emissions from GAINS include transport, industrial and waste emissions. Monthly prior estimates for biomass burning emissions are obtained from GFEDv4.1 (Randerson et al., 2017), excluding agricultural waste burning as it is encompassed in our agriculture emission estimates. Natural emissions were taken from the O-CN GCP, which is the fluxes from unmanaged ("natural") soils. We utilize climatological estimates of ocean emissions from PlankTOM model for ocean prior flux. N_2O emissions from different sources used in the inversion are shown in Figure 5.2. However, the inversion optimises the total emissions combined from all the sources.

This project has received funding from the European Union's Horizon Europe research and innovation programme under grant agreement No 101081395

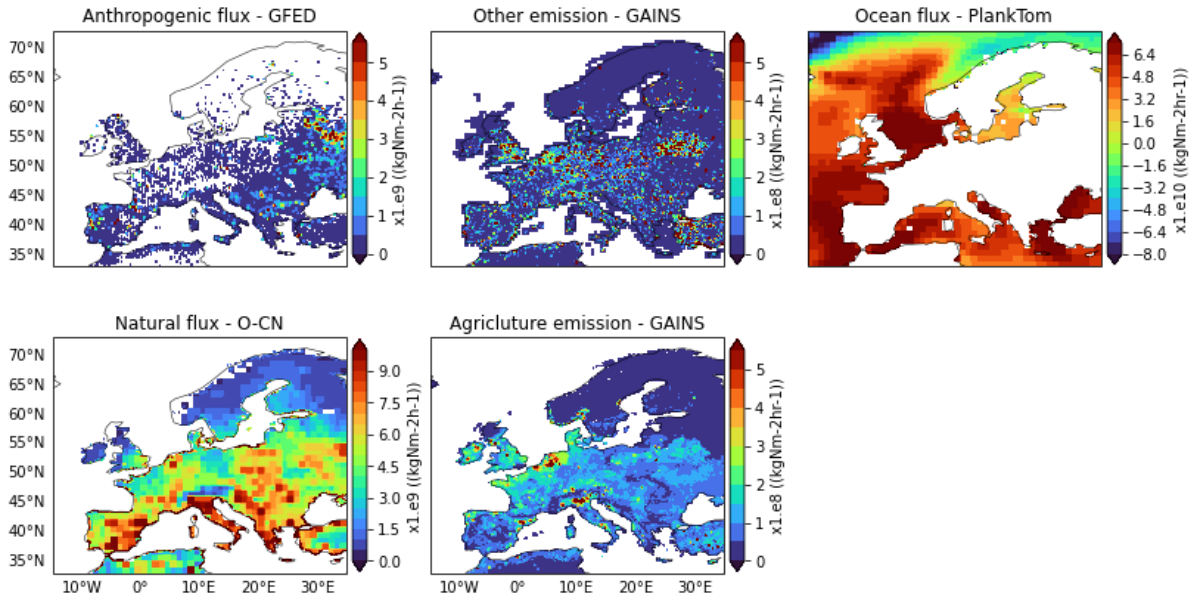

Figure 5.2: Annual mean N_2O emissions. Note that the scales of the maps vary.

5.3 Observations

A new harmonized N_2O observation dataset was compiled for Europe as a collaborative effort between EYE-CLIMA and the Horizon Europe projects, AVENGERS and PARIS. In the inversion, we assimilate data from 19 sites that have valid observations from 2005. Most of the sites have reported data up to at least 2023. The data sources are from the previous European project, InGOS (pre-ICOS), the European network, ICOS, other sites obtained from the World Data Centre for Greenhouse Gases (WDCGG), and the NOAA network (Henne et al., 2024, https://meta.icos-cp.eu/collections/FHIS-w3c_eny9-NDoR7ddvTX). The geographical distribution of sites across Europe is depicted in Figure 5.3 and data density for the inversion period is shown in Figure 5.4. In cases where multiple intake heights were available, such as at the Hohenpeissenberg (HPB) station with intake heights at 131 and 5 meters above ground level, we opted to assimilate data solely from the highest intake height. This approach ensured that the assimilated data represented the uppermost atmospheric layer. We assimilate hourly observations for all the sites.

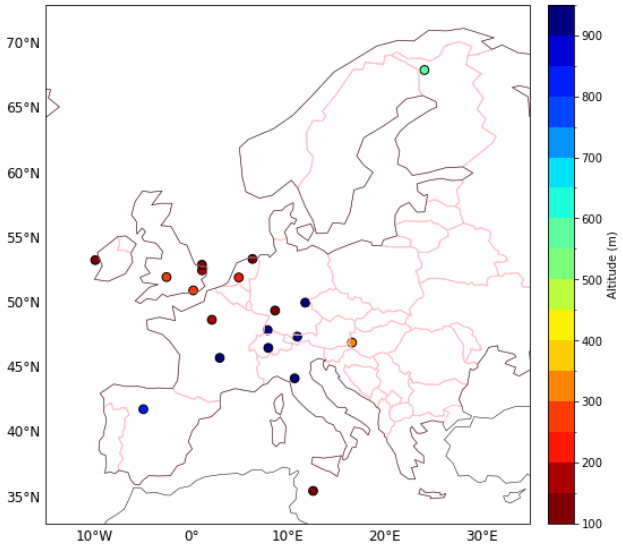

Figure 5.3: Geographical distribution of sites indicating also their altitude

This project has received funding from the European Union's Horizon Europe research and innovation programme under grant agreement No 101081395

The altitude of observation sites vary from sea level to as high as ~2500 masl. However, in the meteorological data used to drive FLEXPART, the orography is only resolved at 0.5° and thus does not capture the true height for the mountain sites (defined here as sites >1000 masl). Hence, the particle release heights in FLEXPART have been adjusted to best represent these sites considering the difference between the true altitude and the altitude in the model orography. Figure 5.4 shows for each site how many months of data are available for a given year for the whole inversion period (2018-2023).

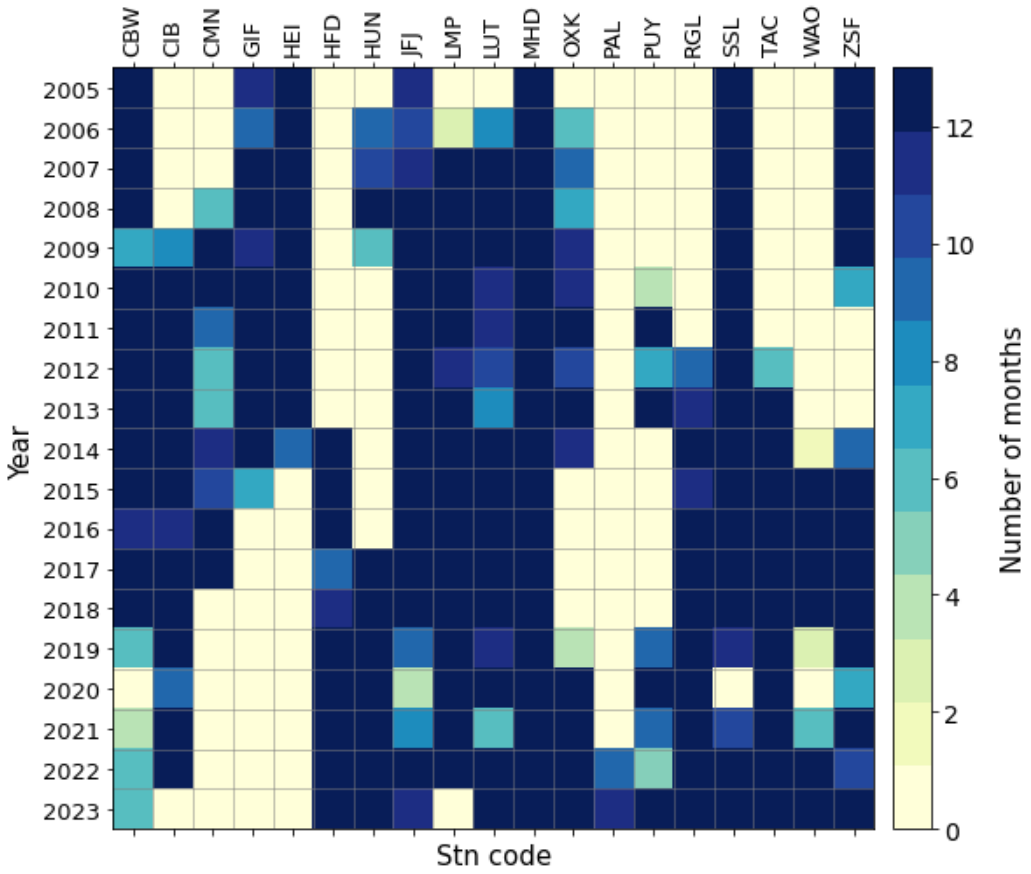

Figure 5.4: Data density in months for each site per year

5.4 Results

5.4.1 Modelled and observed atmospheric N_2O mole fractions

Figure 5.5 show the comparison of daily observed and modelled mole fractions for a few example sites. As expected, after the inversion the modelled mole fractions exhibit an improved alignment with the observations. The mole fractions show a seasonal cycle with an increasing trend from 2015 to 2020. Figure 5.6 shows the statistical analysis of mole fractions across different stations, show casing the predictive performance of models before and after updates. Most stations show relatively high correlation. There are noticeable improvements in some stations from prior to posterior simulations, such as "HFD" and "GIF", where the posterior correlation is significantly better. A few stations, like "PUY" and "RGL", show almost no difference between prior and posterior values. The RMSE values for the posterior simulations (red bars) are generally lower than those for the prior simulations (blue bars) across most stations. The Bias values for the posterior simulations (purple bars) are also lower compared to the prior simulations (green bars) at many stations. This reduction in bias suggests that

This project has received funding from the European Union's Horizon Europe research and innovation programme under grant agreement No 101081395

the systematic errors in the model predictions have been minimized, leading to more reliable results. The consistent decrease in both RMSE and Bias across multiple stations demonstrates the effectiveness of the model updates.

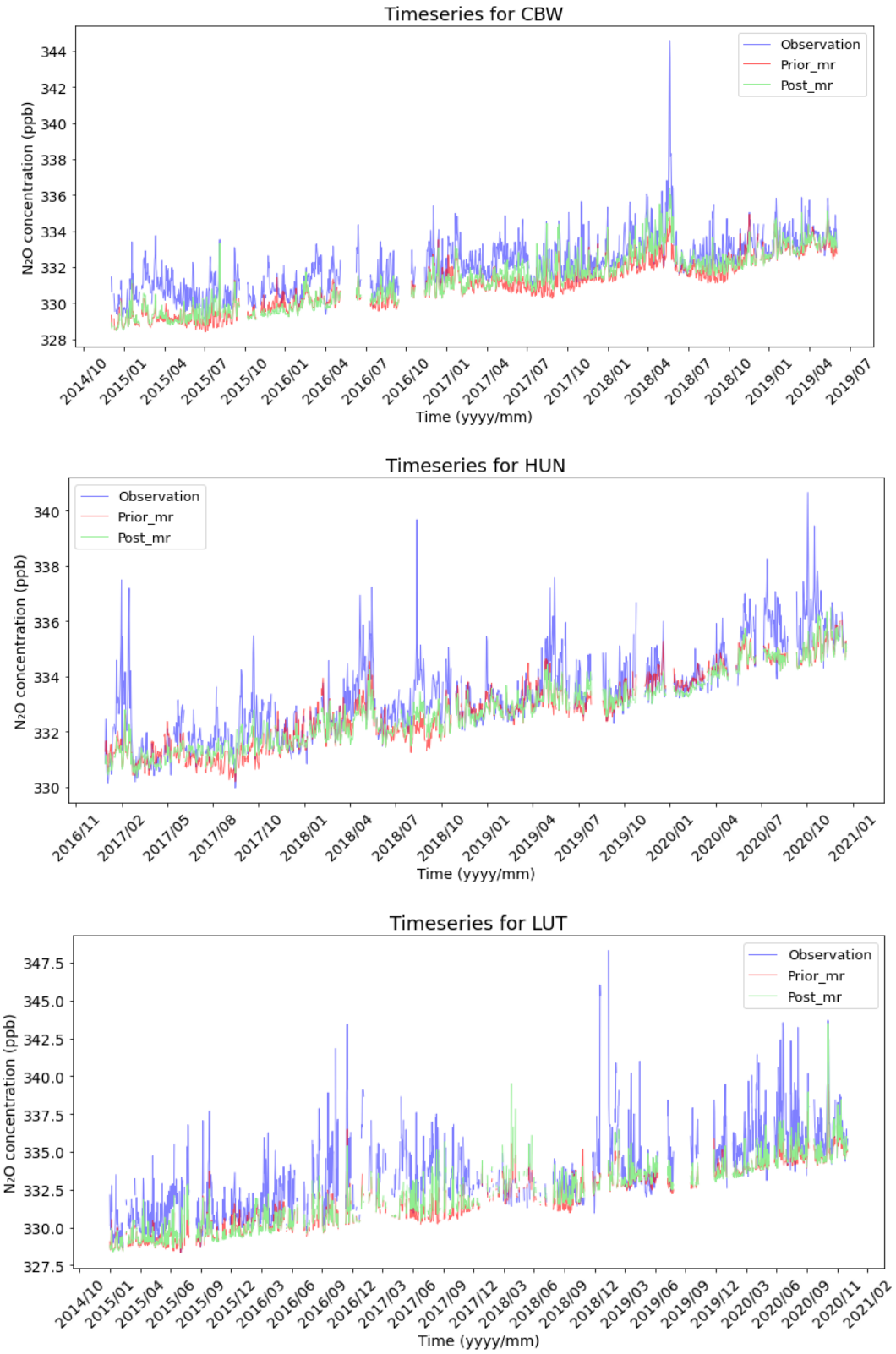

Figure 5.5: Time series of assimilated N_2O mole fractions sampled at different stations used in the inversion. Assimilated measurement (blue), CIF-FLEXPART inversion results a posteriori (green), and a priori (red).

This project has received funding from the European Union's Horizon Europe research and innovation programme under grant agreement No 101081395

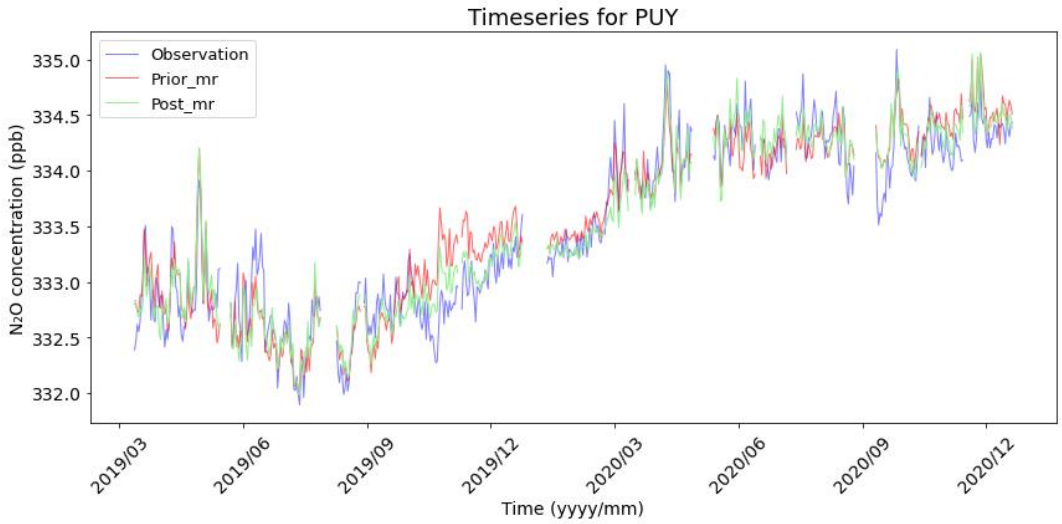

Figure 5.5: Continued.

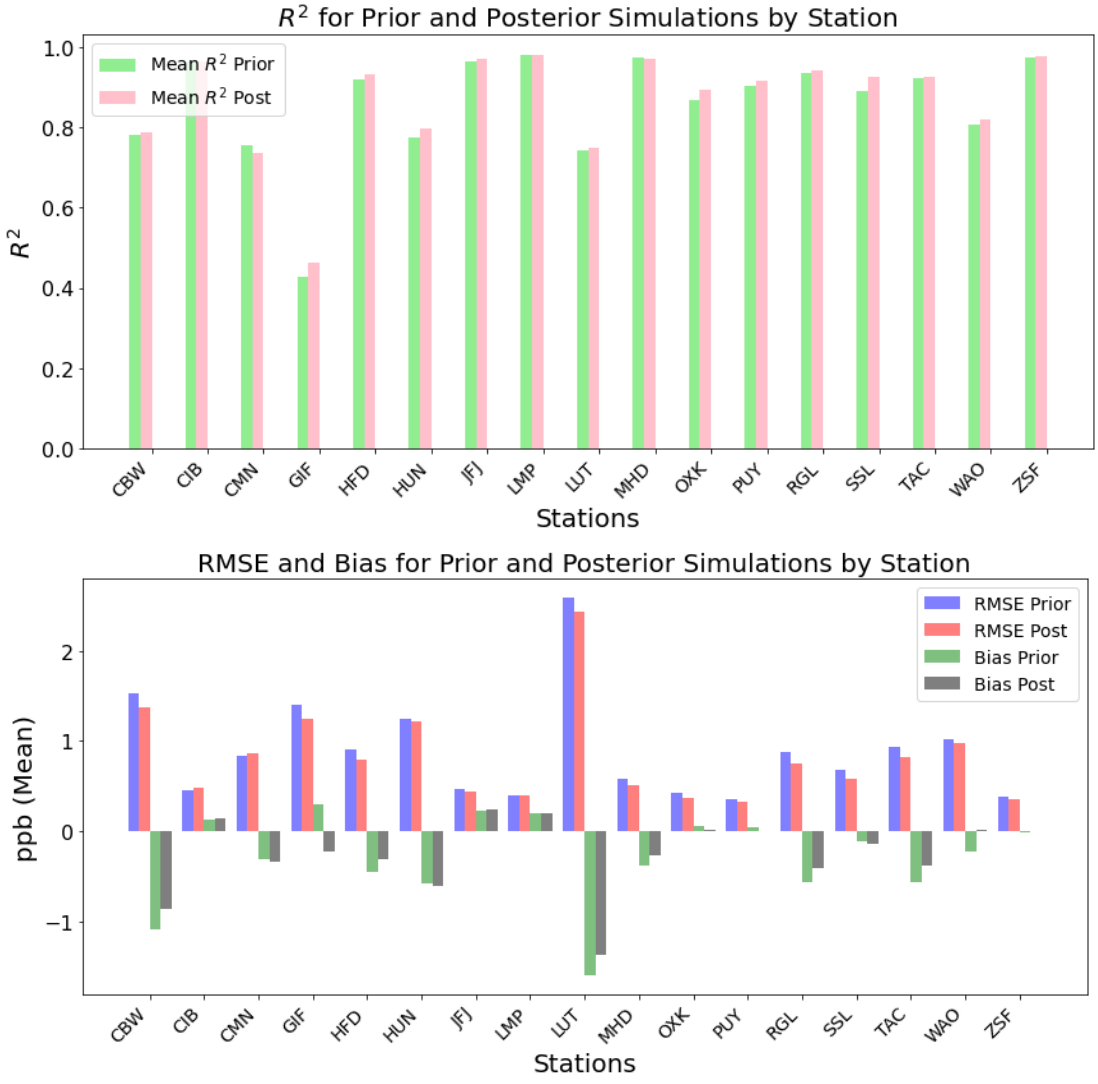

Figure 5.6: Statistical analysis of prior and posterior mole fractions with observations

This project has received funding from the European Union's Horizon Europe research and innovation programme under grant agreement No 101081395

5.4.2 Spatial distribution of prior and posterior emissions

Figure 5.7 shows the spatial distribution of mean N_2O emissions across Europe from 2015 to 2020, revealing regions where significant corrections have been made. Compared to the prior estimates, there are some differences in the intensity and distribution of emissions. Some areas show higher emissions (such as parts of the Netherlands and Germany), while others show reductions. Notable differences are observed in Central and Western Europe. For example, the Netherlands, parts of Germany, and the UK show increases (pink), while parts of France, Switzerland, and Southern Europe show decreases (green). The increase in the emissions relative to the prior in the Netherlands and the UK could be related to agricultural activities.

Figure 5.8 shows the monthly variations in the total annual emissions from 2015-2020. Both the prior and posterior emissions display a clear seasonal cycle, with peaks in emissions typically occurring during early summer (from May to June) and troughs during the winter months. This suggests that N_2O emissions are higher in warmer months and lower in colder months. The total posterior emissions are lower than the prior for all years. Although the seasonal cycle is regular each year, there is some interannual variability in the amplitude, in particular, in 2020, where the posterior emissions peak is the highest of all years.

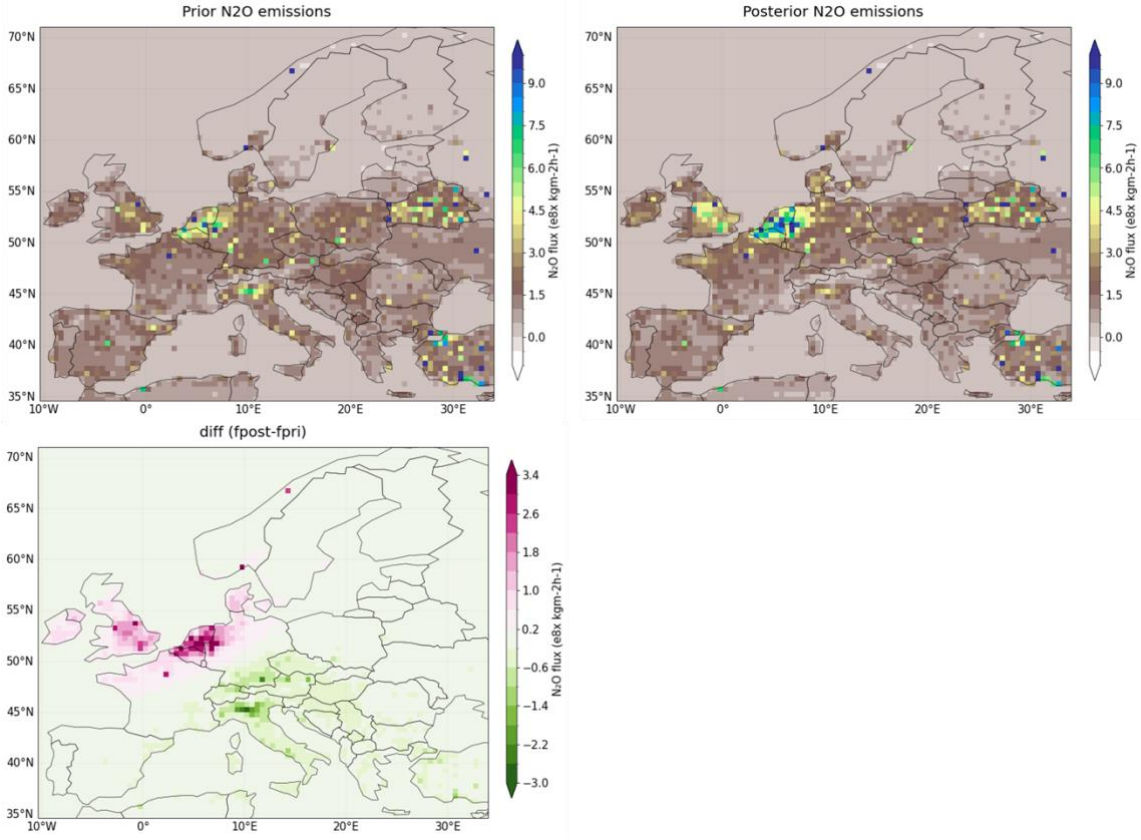

Figure 5.7: Annual mean N_2O estimates from CIF-FLEXPART inversion at the resolution of 0.5°×0.5° from 2015 to 2020: prior (left panel), posterior (middle panel) and posterior increments computed as (posterior – prior) (bottom panel) shown as area fluxes.

This project has received funding from the European Union's Horizon Europe research and innovation programme under grant agreement No 101081395

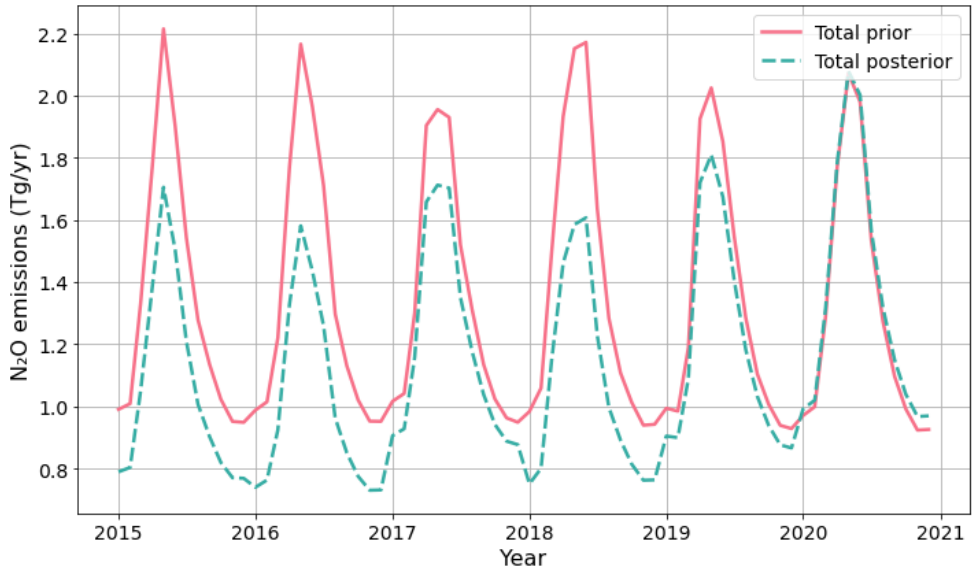

Figure 5.8: Times series of monthly N_2O in Tg(N_2O)/year for the inversion period from 2015 to 2020, for the EU-27+UK+Norway+Switerland area.

6. Deviations from the Description of Action

Task 3.1 aims to perform inversions of CO_2, CH_4 and N_2O over Europe from 2005 to at least 2023. Presently, the inversions are performed from 2005 to 2022 for CO_2, from 2016 to 2022 for CH_4, and from 2015 to 2020 for N_2O. Remaining years of inversions will be completed for the final fluxes in D3.2 due at M28. The CH_4 inversions for this deliverable were run at 1.0° instead of the planned 0.5°, because the development of the model that had been planned to use in this task, i.e., the TM5-MP model with 0.5° resolution, has stalled.

7. Conclusion

Carbon dioxide, methane and nitrous oxide European budgets have been produced using different inversion frameworks. CO_2 inversions using the CIF-CHIMERE model to correct prior estimates of the Net Ecosystem Exchange (NEE) by assimilating surface and OCO-2 satellite observations show that the model significantly improves the fit between simulated and observed CO_2 concentrations, reducing root-mean-square (RMS) errors and biases, with reductions of up to 51% and 92%, respectively, for surface data in July 2015. Inversions generally result in positive corrections in regions like Switzerland and Germany, while satellite-based inversions apply more negative corrections, particularly in Central and Eastern Europe. Seasonally, both surface and satellite inversions show an increased CO_2 uptake in spring and decreased emissions in autumn and winter compared to the prior estimates. European ecosystems act as CO_2 sinks, though there remains variability due to uncertainties in atmospheric transport modeling and boundary conditions. Future analyses are recommended to further refine the NEE estimates and understand the factors influencing CO_2 budgets.

For CH_4, inversion shows that post-optimization results showed improved alignment compared to prior. Performance metrics (R^2, RMSE, and bias) indicated a significant improvement post-optimization (e.g., R^2 increased from 0.43 to 0.77). Spatial maps of CH_4 emissions showing that most biospheric emissions occurred in northern Europe, while anthropogenic emissions concentrated in central and southern regions, especially Germany, the Netherlands, the UK, and France. The inversion increased emissions in high-source areas, notably in northern Europe and certain central regions, except Italy. Total annual

This project has received funding from the European Union's Horizon Europe research and innovation programme under grant agreement No 101081395

CH_4 emissions increased from 20.82 Tg/year (prior) to 25.94 Tg/year (posterior), driven by higher anthropogenic (from 15.00 Tg/year to 19.92 Tg/year) and biospheric emissions (from 1.32 Tg/year to 1.52 Tg/year). Monthly emissions showed a stronger seasonal cycle, with biospheric emissions peaking in late summer and anthropogenic emissions showing a new August maximum after inversion.

N_2O inversions from 2015 to 2020 show an improvement in the fluxes after inversion. Posterior mixing ratios compare better with the observations than prior. Also, the statistical analysis shows an improvement in the flux estimation by reducing the uncertainly. Along with the seasonal cycle, there is an increasing trend of N_2O emissions can be seen from 2015 to 2020. Compared to the prior estimates, there are some differences in the intensity and distribution of emissions. Some areas show higher concentrations (such as parts of the Netherlands and Germany), while others show reductions. Notable differences are observed in Central and Western Europe. For example, the Netherlands, parts of Germany, and the UK show increases, while parts of France, Switzerland, and Southern Europe show decreases. Monthly emissions show a clear seasonal cycle and an increasing trend from 2018.

This project has received funding from the European Union's Horizon Europe research and innovation programme under grant agreement No 101081395

8. References

Berchet, A., Sollum, E., Thompson, R. L., Pison, I., Thanwerdas, J., Broquet, G., Chevallier, F., Aalto, T., Berchet, A., Bergamaschi, P., Brunner, D., Engelen, R., Fortems-Cheiney, A., Gerbig, C., Groot Zwaaftink, C. D., Haussaire, J.-M., Henne, S., Houweling, S., Karstens, U., Kutsch, W. L., Luijkx, I. T., Monteil, G., Palmer, P. I., van Peet, J. C. A., Peters, W., Peylin, P., Potier, E., Rödenbeck, C., Saunois, M., Scholze, M., Tsuruta, A., and Zhao, Y.: The Community Inversion Framework v1.0: a unified system for atmospheric inversion studies, Geoscientific Model Development, 14, 5331–5354, https://doi.org/10.5194/gmd-14-5331-2021, 2021.

Broquet, G., Chevallier, F., Rayner, P., Aulagnier, C., Pison, I., Ramonet, M., Schmidt, M., Vermeulen, A., and Ciais, P.: A European summertime CO 2 biogenic flux inversion at mesoscale from continuous in situ mixing ratio measurements, Journal of Geophysical Research: Atmospheres, 116, D23 303 1–22, https://doi.org/10.1029/2011JD016202, 2011.

Broquet, G., Chevallier, F., Bréon, F.-M., Kadygrov, N., Alemanno, M., Apadula, F., Hammer, S., Haszpra, L., Meinhardt, F., Morguí, J. A., Necki, J., Piacentino, S., Ramonet, M., Schmidt, M., Thompson, R. L., Vermeulen, A. T., Yver, C., and Ciais, P.: Regional inversion of CO2 ecosystem fluxes from atmospheric measurements: reliability of the uncertainty estimates, Atmospheric Chemistry and Physics, 13,175 9039–9056, https://doi.org/10.5194/acp-13-9039-2013, 2013.

Bruhwiler, L., Dlugokencky, E., Masarie, K., Ishizawa, M., Andrews, A., Miller, J., Sweeney, C., Tans, P., and Worthy, D.: CarbonTracker-CH4: An assimilation system for estimating emissions of atmospheric methane, Atmospheric Chemistry and Physics, 14, 8269–8293, https://doi.org/10.5194/acp-14-8269-2014, 2014.

Chevallier, F.: Fluxes of Carbon Dioxide from Managed Ecosystems Estimated by National Inventories Compared to Atmospheric Inverse Modeling, Geophysical Research Letters, 48, e2021GL093 565, https://doi.org/https://doi.org/10.1029/2021GL093565, e2021GL093565 2021GL093565, 2021.

Chevallier, F., Fisher, M., Peylin, P., Serrar, S., Bousquet, P., Bréon, F.-M., Chédin, A., and Ciais, P.: Inferring CO2 sources and sinks from satellite observations: Method and application to TOVS data, Journal of Geophysical Research: Atmospheres, 110, https://doi.org/https://doi.org/10.1029/2005JD006390, 2005.

Chevallier, F., et al., CO_2 surface fluxes at grid point scale estimated from a global 21 year reanalysis of atmospheric measurements, *J. Geophys. Res.*, 115, D21307, doi:10.1029/2010JD013887, 2010.

Chevallier, F., Remaud, M., O'Dell, C. W., Baker, D., Peylin, P., and Cozic, A.: Objective evaluation of surface- and satellite-driven carbon dioxide atmospheric inversions, Atmospheric Chemistry and Physics, 19, 14 233–14 251, https://doi.org/10.5194/acp-19-14233-2019, 2019.

Denier van der Gon, H., Hendriks, C., Kuenen, J., Segers, A., and Visschedijk, A.: TNO Report Description of current temporal emission patterns and sensitivity of predicted AQ for temporal emission patterns EU FP7 MACC deliverable report DD – EM IS1.3, Tech. rep., 2019.

Evensen, G.: The Ensemble Kalman Filter: theoretical formulation and practical implementation, Ocean Dynam., 53, 343–367, doi:10.1007/s10236-003-0036-9, 2003.

Fortems-Cheiney, A., Pison, I., Broquet, G., Dufour, G., Berchet, A., Potier, E., Coman, A., Siour, G., and Costantino, L.: Variational regional inverse modeling of reactive species emissions with PYVAR-CHIMERE-v2019, Geoscientific Model Development, 14, 2939–2957, https://doi.org/10.5194/gmd-14-2939-2021, 2021.

This project has received funding from the European Union's Horizon Europe research and innovation programme under grant agreement No 101081395

Friedlingstein, P., O'Sullivan, M., Jones, M. W., Andrew, R. M., Gregor, L., Hauck, J., Le Quéré, C., Luijkx, I. T., Olsen, A., Peters, G. P., Peters, W., Pongratz, J., Schwingshackl, C., Sitch, S., Canadell, J. G., Ciais, P., Jackson, R. B., Alin, S. R., Alkama, R., Arneth, A., Arora, V. K., Bates, N. R., Becker, M., Bellouin, N., Bittig, H. C., Bopp, L., Chevallier, F., Chini, L. P., Cronin, M., Evans, W., Falk, S., Feely, R. A., Gasser, T., Gehlen, M., Gkritzalis, T., Gloege, L., Grassi, G., Gruber, N., Gürses, O.,Harris, I., Hefner, M., Houghton, R. A., Hurtt, G. C., Iida, Y., Ilyina, T., Jain, A. K., Jersild, A., Kadono, K., Kato, E., Kennedy, D., Klein Goldewijk, K., Knauer, J., Korsbakken, J. I., Landschützer, P., Lefèvre, N., Lindsay, K., Liu, J., Liu, Z., Marland, G., Mayot, N., McGrath, M. J., Metzl, N., Monacci, N. M., Munro, D. R., Nakaoka, S.-I., Niwa, Y., O'Brien, K., Ono, T., Palmer, P. I., Pan, N., Pierrot, D., Pocock, K., Poulter, B., Resplandy, L., Robertson, E., Rödenbeck, C., Rodriguez, C., Rosan, T. M., Schwinger, J., Séférian, R., Shutler, J. D., Skjelvan, I., Steinhoff, T., Sun, Q., Sutton, A. J., Sweeney, C., Takao, S., Tanhua, T., Tans, P. P., Tian, X., Tian, H., Tilbrook, B., Tsujino, H., Tubiello, F., van der Werf, G. R., Walker, A. P., Wanninkhof, R., Whitehead, C., Willstrand Wranne, A., Wright, R., Yuan, W., Yue, C., Yue, X., Zaehle, S., Zeng, J., and Zheng, B.: Global Carbon Budget 2022, Earth System Science Data, 14, 4811–4900, https://doi.org/10.5194/essd-14-4811-2022, 2022.

Koch, F.-T., Gerbig, C., 2023. European anthropogenic CO2 emissions based on EDGARv4.3 and BP statistics 2023 for 2005-2022. https://doi.org/10.18160/RFJD-QV8J

Gilbert, J. and Lemaréchal, C.: Some numerical experiments with variable storage quasi-Newton algorithms, Math. Program., 45, 407–435, https://doi.org/10.1007/BF01589113, 1989.

Hersbach, H., Bell, B., Berrisford, P., Hirahara, S., Hor´anyi, A., Mu˜noz-Sabater, J., Nicolas, J., Peubey, C., Radu, R., Schepers, D., Simmons, A., Soci, C., Abdalla, S., Abellan, X., Balsamo, G., Bechtold, P., Biavati, G., Bidlot, J., Bonavita, M., De Chiara, G., Dahlgren, P., Dee, D., Diamantakis, M., Dragani, R., Flemming, J., Forbes, R., Fuentes, M., Geer, A., Haimberger, L., Healy, S., Hogan, R. J., H´olm, E., Janisková, M., Keeley, S., Laloyaux, P., Lopez, P., Lupu, C., Radnoti, G., de Rosnay, P., Rozum, I., Vamborg, F., Villaume, S., and Th´epaut, J. N.: The ERA5 global reanalysis, Quarterly Journal of the Royal Meteorological Society, 146, 1999–2049, https://doi.org/10.1002/qj.3803, 2020.

ICOS RI, Bergamaschi, P., Colomb, A., De Mazière, M., Emmenegger, L., Kubistin, D., Lehner, I., Lehtinen, K., Lund Myhre, C., Marek, M., Platt, S. M., Plaß-Dülmer, C., Schmidt, M., Apadula, F., Arnold, S., Blanc, P.-E., Brunner, D., Chen, H., Chmura, L., Conil, S., Couret, C., Cristofanelli, P., Delmotte, M., Forster, G., Frumau, A., Gheusi, F., Hammer, S., Haszpra, L., Heliasz, M., Henne, S., Hoheisel, A., Kneuer, T., Laurila, T., Leskinen, A., Leuenberger, M., Levin, I., Lindauer, M., Lopez, M., Lunder, C., Mammarella, I., Manca, G., Manning, A., Marklund, P., Martin, D., Meinhardt, F., Müller-Williams, J., Necki, J., O'Doherty, S., Ottosson-Löfvenius, M., Philippon, C., Piacentino, S., Pitt, J., Ramonet, M., Rivas-Soriano, P., Scheeren, B., Schumacher, M., Sha, M. K., Spain, G., Steinbacher, M., Sørensen, L. L., Vermeulen, A., Vítková, G., Xueref-Remy, I., di Sarra, A., Conen, F., Kazan, V., Roulet, Y.-A., Biermann, T., Heltai, D., Hensen, A., Hermansen, O., Komínková, K., Laurent, O., Levula, J., Pichon, J.-M., Smith, P., Stanley, K., Trisolino, P., ICOS Carbon Portal, ICOS Atmosphere Thematic Centre, ICOS Flask And Calibration Laboratory, and ICOS Central Radiocarbon Laboratory: European Obspack compilation of atmospheric carbon dioxide data from ICOS and non-ICOS European stations for the period 1972-2023; obspackco2466GLOBALVIEW plus v8.02023-04-6, https: //doi.org/10.18160/CEC4 – CAGK, 2023.

Janssens-Maenhout, G., Crippa, M., Guizzardi, D., Muntean, M., Schaaf, E., Dentener, F., Bergamaschi, P., Pagliari, V., Olivier, J. G. J., Peters, J. A. H. W., van Aardenne, J. A., Monni, S., Doering, U., Petrescu, A. M. R., Solazzo, E., and Oreggioni, G. D.: EDGAR v4.3.2 Global Atlas of the three major

This project has received funding from the European Union's Horizon Europe research and innovation programme under grant agreement No 101081395

greenhouse gas emissions for the period 1970–2012, Earth System Science Data, 11, 959–1002, https://doi.org/10.5194/essd-11-959-2019, 2019.

Jung, M., Schwalm, C., Migliavacca, M., Walther, S., Camps-Valls, G., Koirala, S., Anthoni, P., Besnard, S., Bodesheim, P., Carvalhais, N., Chevallier, F., Gans, F., Goll, D. S., Haverd, V., Köhler, P., Ichii, K., Jain, A. K., Liu, J., Lombardozzi, D., Nabel, J. E. M. S., Nelson, J. A., O'Sullivan, M., Pallandt, M., Papale, D., Peters, W., Pongratz, J., Rödenbeck, C., Sitch, S., Tramontana, G., Walker, A., Weber, U., and Reichstein, M.: Scaling carbon fluxes from eddy covariance sites to globe: synthesis and evaluation of the FLUXCOM approach, Biogeosciences, 17, 1343–1365, https://doi.org/10.5194/bg-17-1343-2020, 2020.

Jöckei, P., Tost, H., Pozzer, A., Brühl, C., Buchholz, J., Ganzeveld, L., Hoor, P., Kerkweg, A., Lawrence, M. G., Sander, R., Steil, B., Stiller, G., Tanarhte, M., Taraborrelli, D., Van Aardenne, J., and Lelieveld, J.: The atmospheric chemistry general circulation model ECHAM5/MESSy1: Consistent simulation of ozone from the surface to the mesosphere, Atmospheric Chemistry and Physics, 6, 5067–5104, https://doi.org/10.5194/acp-6-5067-2006, 2006.

Kangasaho, V., Tsuruta, A., Backman, L., M ̈akinen, P., Houweling, S., Segers, A., Krol, M., Dlugokencky, E. J., Michel, S., White, J. W. C., and Aalto, T.: The Role of Emission Sources and Atmospheric Sink in the Seasonal Cycle of CH4 and δ13-CH4: Analysis Based on the Atmospheric Chemistry Transport Model TM5, Atmosphere, 13, 888, https://doi.org/10.3390/atmos13060888, 2022.

Kountouris, P., Gerbig, C., Totsche, K.-U., Dolman, A. J., Meesters, A. G. C. A., Broquet, G., Maignan, F., Gioli, B., Montagnani, L., and Helfter, C.: An objective prior error quantification for regional atmospheric inverse applications, Biogeosciences, 12, 7403–7421, https://doi.org/10.5194/bg-12-7403-2015, 2015.

Krinner, G., Viovy, N., de Noblet-Ducoudré, N., Ogée, J., Polcher, J., Friedlingstein, P., Ciais, P., Sitch, S., and Prentice, I. C.: A dynamic global vegetation model for studies of the coupled atmosphere-biosphere system, Global Biogeochemical Cycles, 19, https://doi.org/https://doi.org/10.1029/2003GB002199, 2005.

Krol, M., Houweling, S., Bregman, B., van den Broek, M., Segers, A., van Velthoven, P., Peters, W., Dentener, F., Bergamaschi, P., Broek, M. V. D., Segers, A., Velthoven, P. V., Peters, W., Dentener, F., van den Broek, M., Segers, A., van Velthoven, P., Peters, W., Dentener, F., Bergamaschi, P., Broek, M. V. D., Segers, A., Velthoven, P. V., Peters, W., and Dentener, F.: The two-way nested global chemistry-transport zoom model TM5: algorithm and applications, Atmospheric Chemistry and Physics, 5, 417–432, https://doi.org/10.5194/acp-5-417-2005, 2005.

Lienert, S. and Joos, F.: A Bayesian ensemble data assimilation to constrain model parameters and land-use carbon emissions, Biogeosciences, 15, 2909–2930, https://doi.org/10.5194/bg-15-2909-2018, 2018.

Mahadevan, P., Wofsy, S. C., Matross, D. M., Xiao, X., Dunn, A. L., Lin, J. C., Gerbig, C., Munger, J. W., Chow, V. Y., and Gottlieb, E. W.: A satellite-based biosphere parameterization for net ecosystem CO2 exchange: Vegetation Photosynthesis and Respiration Model (VPRM), Global Biogeochemical Cycles, 22, https://doi.org/https://doi.org/10.1029/2006GB002735, 2008.

Mailler, S., Menut, L., Khvorostyanov, D., Valari, M., Couvidat, F., Siour, G., Turquety, S., Briant, R., Tuccella, P., Bessagnet, B., Colette, A., Létinois, L., Markakis, K., and Meleux, F.: CHIMERE-2017: from urban to hemispheric chemistry-transport modeling, Geoscientific Model Development, 10, 2397–2423, https://doi.org/10.5194/gmd-10-2397-2017, 2017.

This project has received funding from the European Union's Horizon Europe research and innovation programme under grant agreement No 101081395

McGrath, M. J., Petrescu, A. M. R., Peylin, P., Andrew, R. M., Matthews, B., Dentener, F., Balkovi˘c, J., Bastrikov, V., Becker, M., Broquet, G., Ciais, P., Fortems, A., Ganzenmüller, R., Grassi, G., Harris, I., Jones, M., Knauer, J., Kuhnert, M., Monteil, G., Munassar, S., Palmer, P. I., Peters, G. P., Qiu, C., Schelhaas, M.-J., Tarasova, O., Vizzarri, M., Winkler, K., Balsamo, G., Berchet, A., Briggs, P., Brockmann, P., Chevallier, F., Conchedda, G., Crippa, M., Dellaert, S., Denier van der Gon, H. A. C., Filipek, S., Friedlingstein, P., Fuchs, R., Gauss, M., Gerbig, C., Guizzardi, D., Günther, D., Houghton, R. A., Janssens-Maenhout, G., Lauerwald, R., Lerink, B., Luijkx, I. T., Moulas, G., Muntean, M., Nabuurs, G.-J., Paquirissamy, A., Perugini, L., Peters, W., Pilli, R., Pongratz, J., Regnier, P., Scholze, M., Serengil, Y., Smith, P., Solazzo, E., Thompson, R. L., Tubiello, F. N., Vesala, T., and Walther, S.: The consolidated European synthesis of CO2 emissions and removals for EU27 and UK: 1990–2020, Earth System Science Data Discussions, 2023, 1–123, https://doi.org/10.5194/essd-2022-412, 2023.

Menut, L., Bessagnet, B., Khvorostyanov, D., Beekmann, M., Blond, N., Colette, A., Coll, I., Curci, G., Foret, G., Hodzic, A., Mailler, S., Meleux, F., Monge, J.-L., Pison, I., Siour, G., Turquety, S., Valari, M., Vautard, R., and Vivanco, M. G. : CHIMERE 2013: a model for regional atmospheric composition modelling, Geoscientific Model Development, 6, 981–1028, https://doi.org/10.5194/gmd-6-981-2013, 2013.

Monteil, G., Broquet, G., Scholze, M., Lang, M., Karstens, U., Gerbig, C., Koch, F.-T., Smith, N. E., Thompson, R. L., Luijkx, I. T., White, E., Meesters, A., Ciais, P., Ganesan, A. L., Manning, A., Mischurow, M., Peters, W., Peylin, P., Tarniewicz, J., Rigby, M., Rödenbeck, C., Vermeulen, A., and Walton, E. M.: The regional European atmospheric transport inversion comparison, EUROCOM: first results on European-wide terrestrial carbon fluxes for the period 2006–2015, Atmospheric Chemistry and Physics, 20, 12 063–12 091, https://doi.org/10.5194/acp-20-12063-2020, 2020.

Munassar, S., Rödenbeck, C., Koch, F.-T., Totsche, K. U., Gałkowski, M., Walther, S., and Gerbig, C.: Net ecosystem exchange (NEE) estimates 2006–2019 over Europe from a pre-operational ensemble-inversion system, Atmospheric Chemistry and Physics, 22, 7875–7892, https://doi.org/10.5194/acp-22-7875-2022, 2022.

O'Dell, C. W., Eldering, A., Wennberg, P. O., Crisp, D., Gunson, M. R., Fisher, B., Frankenberg, C., Kiel, M., Lindqvist, H., Mandrake, L., Merrelli, A., Natraj, V., Nelson, R. R., Osterman, G. B., Payne, V. H., Taylor, T. E., Wunch, D., Drouin, B. J., Oyafuso, F., Chang, A., McDuffie, J., Smyth, M., Baker, D. F., Basu, S., Chevallier, F., Crowell, S. M. R., Feng, L., Palmer, P. I., Dubey, M., García, O. E., Griffith, D. W. T., Hase, F., Iraci, L. T., Kivi, R., Morino, I., Notholt, J., Ohyama, H., Petri, C., Roehl, C. M., Sha, M. K., Strong, K., Sussmann, R., Te, Y., Uchino, O., and Velazco, V. A.: Improved retrievals of carbon dioxide from Orbiting Carbon Observatory-2 with the version 8 ACOS algorithm, Atmospheric Measurement Techniques, 11, 6539–6576, https://doi.org/10.5194/amt-11-6539-2018, 2018.

Peters, W., Miller, J. B., Whitaker, J., Denning, A. S., Hirsch, A., Krol, M. C., Zupanski, D., Bruhwiler, L., and Tans, P. P.: An ensemble data assimilation system to estimate CO2 surface fluxes from atmospheric trace gas observations, Journal of Geophysical Research Atmospheres, 110, 1–18, https://doi.org/10.1029/2005JD006157, 2005.

Petrescu, A. M. R., McGrath, M. J., Andrew, R. M., Peylin, P., Peters, G. P., Ciais, P., Broquet, G., Tubiello, F. N., Gerbig, C., Pongratz, J., Janssens-Maenhout, G., Grassi, G., Nabuurs, G.-J., Regnier, P., Lauerwald, R., Kuhnert, M., Balkovič, J., Schelhaas, M.-J., Denier van der Gon, H. A. C., Solazzo, E., Qiu, C., Pilli, R., Konovalov, I. B., Houghton, R. A., Günther, D., Perugini, L., Crippa, M., Ganzenmüller, R., Luijkx, I. T., Smith, P., Munassar, S., Thompson, R. L., Conchedda, G., Monteil, G., Scholze, M., Karstens, U., Brockmann, P., and Dolman, A. J.: The consolidated European synthesis of CO_2

This project has received funding from the European Union's Horizon Europe research and innovation programme under grant agreement No 101081395

emissions and removals for the European Union and United Kingdom: 1990–2018, Earth Syst. Sci. Data, 13, 2363–2406, https://doi.org/10.5194/essd-13-2363-2021, 2021.

Rödenbeck, C., Bakker, D. C. E., Metzl, N., Olsen, A., Sabine, C., Cassar, N., Reum, F., Keeling, R. F., and Heimann, M.: Interannual sea–air CO2 flux variability from an observation-driven ocean mixed-layer scheme, Biogeosciences, 11, 4599– 4613, https://doi.org/10.5194/bg-11-4599-2014, 2014.

Sasakawa, M., Shimoyama, K., Machida, T., Tsuda, N., Suto, H., Arshinov, M., Davydov, D., Fofonov, A., Krasnov, O., Saeki, T., Koyama, Y., and Maksyutov, S.: Continuous measurements of methane from a tower network over Siberia, Tellus, Series B: Chemical and Physical Meteorology, 62, 403–416, https://doi.org/10.1111/j.1600-0889.2010.00494.x, 2010.

Saunois, M., Stavert, A. R., Poulter, B., Bousquet, P., Canadell, J. G., Jackson, R. B., Raymond, P. A., Dlugokencky, E. J., Houweling, S., Patra, P. K., Ciais, P., Arora, V. K., Bastviken, D., Bergamaschi, P., Blake, D. R., Brailsford, G., Bruhwiler, L., Carlson, K. M., Carrol, M., Castaldi, S., Chandra, N., Crevoisier, C., Crill, P. M., Covey, K., Curry, C. L., Etiope, G., Frankenberg, C., Gedney, N., Hegglin, M. I., Höglund-Isaksson, L., Hugelius, G., Ishizawa, M., Ito, A., Janssens-Maenhout, G., Jensen, K. M., Joos, F., Kleinen, T., Krummel, P. B., Langenfelds, R. L., Laruelle, G. G., Liu, L., Machida, T., Maksyutov, S., McDonald, K. C., McNorton, J., Miller, P. A., Melton, J. R., Morino, I., Müller, J., Murguia-Flores, F., Naik, V., Niwa, Y., Noce, S., O'Doherty, S., Parker, R. J., Peng, C., Peng, S., Peters, G. P., Prigent, C., Prinn, R., Ramonet, M., Regnier, P., Riley, W. J., Rosentreter, J. A., Segers, A., Simpson, I. J., Shi, H., Smith, S. J., Steele, L. P., Thornton, B. F., Tian, H., Tohjima, Y., Tubiello, F. N., Tsuruta, A., Viovy, N., Voulgarakis, A., Weber, T. S., van Weele, M., van der Werf, G. R., Weiss, R. F., Worthy, D., Wunch, D., Yin, Y., Yoshida, Y., Zhang, W., Zhang, Z., Zhao, Y., Zheng, B., Zhu, Q., Zhu, Q., and Zhuang, Q.: The Global Methane Budget 2000–2017, Earth System Science Data, 12, 1561–1623, https://doi.org/10.5194/essd-12-1561-2020, 2020.

Saunois, M., Martinez, A., Poulter, B., Zhang, Z., Raymond, P. A., Pierre Regnier, Canadell, J. G., Jackson, R. B., Patra, P. K., Bousquet, P., Philippe Ciais, Dlugokencky, E. J., Lan, X., Allen, G. H., Bastviken, D., Beerling, J., D., Belikov, D. A., Blake, D. R., Castaldi, S., Crippa, M., Deemer, B. R., Dennison, F., Etiope, G., Gedney, N., Höglund-Isaksson, L., Holgerson, M. A., Hopcroft, P. O., Hugelius, G., Ito, A., Jain, A. K., Janardanan, R., Johnson, M. S., Kleinen, T., Krummel, P. B., Lauerwald, R., Li, T., Liu, X., McDonald, K. C., Melton, J. R., Mühle, J., Müller, J., Murguia-Flores, F., Niwa, Y., Noce, S., Pan, S., Parker, R. J., Peng, C., Ramonet, M., Riley, W. J., Rocher-Ros, G., Rosentreter, J. A., Sasakawa, M., Segers, A., Smith, S. J., Stanley, E. H., Thanwerdas, J., Tian, H., Tsuruta, A., Tubiello, F. N., Weber, T. S., Werf, G. R. v. d., Worthy, D. E. J., Xi, Y., Yoshida, Y., Zhang, W., Bo Zheng, Zhu, Q., Zhu, Q., and Zhuang, Q.: Global Methane Budget 2000-2020, Earth System Science Data Discussions, pp. 1–147, https://doi.org/10.5194/essd-2024-115, 2024.

Schuldt, K. N., Aalto, T., Andrews, A., Aoki, S., Arduini, J., Baier, B., Bergamaschi, P., Biermann, T., Biraud, S. C., Boenisch, H., Brailsford, G., Chen, H., Colomb, A., Conil, S., Cristofanelli, P., Cuevas, E., Daube, B., Davis, K., Mazière, M. D., Delmotte, M., Desai, A., DiGangi, J. P., Dlugokencky, E., Elkins, J. W., Emmenegger, L., Fischer, M. L., Gatti, L. V., Gehrlein, T., Gerbig, C., Gloor, E., Goto, D., Haszpra, L., Hatakka, J., Heimann, M., Heliasz, M., Hermanssen, O., Hintsa, E., Holst, J., Ivakhov, V., Jaffe, D., Joubert, W., Kang, H.-Y., Karion, A., Kazan, V., Keronen, P., Ko, M.-Y., Kominkova, K., Kort, E., Kozlova, E., Krummel, P., Kubistin, D., Labuschagne, C., Langenfelds, R., Laurent, O., Laurila, T., Lauvaux, T., Lee, J., Lee, H., Lee, C.-H., Lehner, I., Leppert, R., Leuenberger, M., Lindauer, M., Loh, Z., Lopez, M., Machida, T., Mammarella, I., Manca, G., Marek, M. V., Martin, M. Y., Matsueda, H., McKain, K., Miles, N., Miller, C. E., Miller, J. B., Moore, F., Morimoto, S., Munro, D., Myhre, C. L., Mölder, M., Müller-Williams, J., Nichol, S., Niwa, Y., O'Doherty, S., Obersteiner, F., Piacentino, S.,

This project has received funding from the European Union's Horizon Europe research and innovation programme under grant agreement No 101081395

Pichon, J. M., Pittman, J., Plass-Duelmer, C., Ramonet, M., Richardson, S., Rivas, P. P., Saito, K., Santoni, G., Sasakawa, M., Scheeren, B., Schuck, T., Schumacher, M., Seifert, T., Sha, M. K., Shepson, P., Sloop, C. D., Smith, P., Steinbacher, M., Stephens, B., Sweeney, C., Timas, H., Torn, M., Trisolino, P., Turnbull, J., Tørseth, K., Viner, B., Vitkova, G., Watson, A., Wofsy, S., Worsey, J., Worthy, D., Zahn, A., and Sarra, A. G. d.: Multi-laboratory compilation of atmospheric carbon dioxide data for the period 1983-2020; obspack ch4 1 GLOBALVIEWplus v4.0 2021-10-14, https://doi.org/10.25925/20211001, 2021.

Sitch, S., Friedlingstein, P., Gruber, N., Jones, S. D., Murray-Tortarolo, G., Ahlström, A., Doney, S. C., Graven, H., Heinze, C., Huntingford, C., Levis, S., Levy, P. E., Lomas, M., Poulter, B., Viovy, N., Zaehle, S., Zeng, N., Arneth, A., Bonan, G., Bopp, L., Canadell, J. G., Chevallier, F., Ciais, P., Ellis, R., Gloor, M., Peylin, P., Piao, S. L., Le Quéré, C., Smith, B., Zhu, Z., and Myneni, R.: Recent trends and drivers of regional sources and sinks of carbon dioxide, Biogeosciences, 12, 653–679, https://doi.org/10.5194/bg-12-653-2015, 2015.

Steinbach, J., Gerbig, C., Rödenbeck, C., Karstens, U., Minejima, C., and Mukai, H.: The CO2 release and Oxygen uptake from Fossil Fuel Emission Estimate (COFFEE) dataset: effects from varying oxidative ratios, Atmospheric Chemistry and Physics, 11, 6855–6870, https://doi.org/10.5194/acp-11-6855-2011, 2011

Tenkanen, M. K., Tsuruta, A., Tyystjärvi, V., Törmä, M., Autio, I., Haakana, M., Tuomainen, T., Leppänen, A., Markkanen, T., Raivonen, M., Niinistö, S., Arslan, A. N., and Aalto, T.: Using Atmospheric Inverse Modelling of Methane Budgets with Copernicus Land Water and Wetness Data to Detect Land Use-Related Emissions, Remote Sensing, 16, 124, https://doi.org/10.3390/rs16010124, 2023.

Thompson, R. L., Broquet, G., Gerbig, C., Koch, T., Lang, M., Monteil, G., Munassar, S., Nickless, A., Scholze, M., Ramonet, M., Karstens, U., van Schaik, E., Wu, Z., and Rödenbeck, C.: Changes in net ecosystem exchange over Europe during the 2018 drought based on atmospheric observations, Philos. T. R. Soc. B, 375, 20190512, 2020.

Tsuruta, A., Aalto, T., Backman, L., Hakkarainen, J., van der Laan-Luijkx, I. T., Krol, M. C., Spahni, R., Houweling, S., Laine, M., Dlugokencky, E., Gomez-Pelaez, A. J., van der Schoot, M., Langenfelds, R., Ellul, R., Arduini, J., Apadula, F., Gerbig, C., Feist, D. G., Kivi, R., Yoshida, Y., and Peters, W.: Global methane emission estimates for 2000–2012 from CarbonTracker Europe-CH4 v1.0, Geoscientific Model Development, 10, 1261–1289, https://doi.org/10.5194/gmd-10-1261-2017, 2017.

Tsuruta, A., Aalto, T., Backman, L., Krol, M. C., Peters, W., Lienert, S., Joos, F., Miller, P. A., Zhang, W., Laurila, T., Hatakka, J., Leskinen, A., Lehtinen, K. E. J., Peltola, O., Vesala, T., Levula, J., Dlugokencky, E., Heimann, M., Kozlova, E., Aurela, M., Lohila, A., Kauhaniemi, M., and Gomez-Pelaez, A. J.: Methane budget estimates in Finland from the CarbonTracker Europe-CH4 data assimilation system, Tellus B: Chemical and Physical Meteorology, 71, 1–20, https://doi.org/10.1080/16000889.2018.1565030, 2019.

van der Laan-Luijkx, I. T., van der Velde, I. R., van der Veen, E., Tsuruta, A., Stanislawska, K., Babenhauserheide, A., Zhang, H. F., Liu, Y., He, W., Chen, H., Masarie, K. A., Krol, M. C., and Peters, W.: The CarbonTracker Data Assimilation Shell (CTDAS) v1.0: implementation and global carbon balance 2001–2015, Geoscientific Model Development, 10, 2785–2800, https://doi.org/10.5194/gmd-10-2785-2017, 2017.

van der Werf, G. R., Randerson, J. T., Giglio, L., van Leeuwen, T. T., Chen, Y., Rogers, B. M., Mu, M., van Marle, M. J. E., Morton, D. C., Collatz, G. J., Yokelson, R. J., and Kasibhatla, P. S.: Global fire

This project has received funding from the European Union's Horizon Europe research and innovation programme under grant agreement No 101081395

emissions estimates during 1997–2016, Earth System Science Data, 9, 697–720, https://doi.org/10.5194/essd-9-697-2017, 2017.

Weber, T., Wiseman, N. A., and Kock, A.: Global ocean methane emissions dominated by shallow coastal waters, Nature Communications, 10, 4584, https://doi.org/10.1038/s41467-019-12541-7, 2019.

This project has received funding from the European Union's Horizon Europe research and innovation programme under grant agreement No 101081395

https://eyeclima.eu

BRUSSELS, 19 09 2024

Funded by the European Union. Views and opinions expressed are however those of the author(s) only and do not necessarily reflect those of the European Union. Neither the European Union nor the granting authority can be held responsible for them.

This project has received funding from the European Union's Horizon Europe research and innovation programme under grant agreement No 101081395